Petro-geochemical constraints on the source and evolution of magmas at El Misti volcano (Peru)

Marco Rivera, Hervé Martin, Jean-Luc Le Pennec, Jean-Claude Thouret, Alain Gourgaud, Marie-Christine Gerbe

Petro-geochemical constraints on the source and evolution of magmas at El Misti volcano (Peru)

Marco Rivera [a,b,*], Hervé Martin [b], Jean-Luc Le Pennec [b], Jean-Claude Thouret [b], Alain Gourgaud [b], Marie-Christine Gerbe [c]

[a] Observatorio Vulcanológico del INGEMMET (Dirección de Geología Ambiental y Riesgo Geológico), Urb. Magisterial B-16, Yanahuara, Arequipa, Peru
[b] Université Clermont Auvergne, Laboratoire Magmas et Volcans UMR 6524 CNRS & IRD R163, OPGC, Campus Universitaire des Cézeaux, 6 Avenue Blaise Pascal, TSA 60026 - CS 60026, 63178 Aubière Cedex, France
[c] Université Jean Monnet, Laboratoire Magmas et Volcans, 23 rue Dr. Paul Michelon, 42023 Saint Etienne, France

El Misti volcano, a large and hazardous edifice of the Andean Central Volcanic Zone (CVZ) of southern Peru, con-sists of four main growth stages. Misti 1 (>112 ka) is an old stratovolcano partly concealed by two younger stratocones (Misti 2, 112–40 ka; Misti 3, 38–11 ka), capped in turn by a recent summit cone (Misti 4, <11 ka). In order to gain insights into magma composition controls on eruptive behaviour through time at El Misti, we have conducted a petrological and geochemical study of selected rock samples from the main growth stages of the volcano. Whole rock compositions range from andesite to rhyolite and belong to a medium to high-K calk-alkaline magmatic suite. El Misti samples are characterised by high large-ion lithophile elements, but low concen-trations of high field strength elements, and heavy rare earth elements, consistent with a subduction zone setting. The $^{87}Sr/^{86}Sr$ (0.70715–0.70882) and $^{143}Nd/^{144}Nd$ (0.511983–0.512277) isotope ratios suggest that magma com-position is significantly affected by contamination and/or assimilation processes during their evolution, likely due to the presence of thick (65–70 km) continental crust beneath the CVZ in southern Peru. Geochemical evidence indicates that magmatic evolution is mostly controlled by Assimilation–Fractional Crystallisation (AFC) mecha-nisms. Modelling reveals a mass-assimilated/mass-fractionated ratio (ρ) ≤ 2.2, which suggests an assimilated crust fraction below 14 wt.% on average. Our isotopic data clearly identify the Proterozoic "Charcani gneiss" base-ment as the main contaminant. Both contamination and assimilation processes peaked at ~30 wt.%, during the Misti 3 stage when rhyolites were generated. We ascribe the general depletion in HREE and Y and elevated La/Yb and Sr/Y ratios in El Misti samples to the enrichment of the mantle wedge source of the parental magmas by a felsic melt of adakitic composition and hydrous fluids. Our work highlights that El Misti's magmatic system has remained relatively homogeneous since at least 0.12 Ma, with a marked influence of the contaminating crust in the Late Pleistocene Misti 3 stage, which resulted in highly explosive eruptions. Andesitic-dacitic compositions are dominant in the Holocene and historical Misti 4 stage, and are expected for future volcanic events at El Misti.

1. Introduction

Since the Jurassic, widespread magmatism has developed along the Andean margin as a result of the Nazca Plate subducting beneath the South American continent. Throughout the Cenozoic, the segmentation of the subduction regime has led to the formation of four volcanic provinces known as the Northern, Central, Southern and Austral Volcanic Zones of the Andes (Thorpe et al., 1982; Fig. 1a). Offshore from southern Peru, the 44 Ma-old oceanic Nazca Plate (anomaly 20 according to Herron, 1972) converges with the South American plate at N80° and an average velocity of 5–7 cm/yr (Norabuena et al., 1998). The Central Volcanic Zone (CVZ), which extends from 16° S (Southern Peru) to 28° S (Northern Chile), consists primarily of large silicic systems and andesitic-dacitic composite volcanoes, with some subsidiary monogenetic fields (de Silva and Francis, 1991; Delacour et al., 2007; Stern, 2004; Wörner et al., 2000).

Quaternary erupted lavas in the CVZ are characterised by high $^{87}Sr/^{86}Sr$ and $\delta^{18}O$ ratios (typically >0.70534 and 8–12‰, respectively) and low $^{207}Pb/^{204}Pb$ (15.55–15.65) and ε_{Nd} (−2 to −12), in conjunction with low heavy rare earth elements (HREE) and Y contents (Davidson et al., 1991; de Silva et al., 2006; Delacour et al., 2007; Feeley and Davidson, 1994; Haschke et al., 2006; Kay et al., 2010; Kiebala, 2008; Mamani et al., 2010; Thouret et al., 2005; Wörner et al., 1988).

Previous work on magma genesis and evolution in the CVZ have revealed complex processes that combine initial melt production with tranfers of metasomatic fluids and/or felsic melts into the mantle wedge, and subsequent differentiation through mechanisms such as MASH (melting, assimilation, storage and homogenisation), fractional crystallisation, AFC (Assimilation–Fractional Crystallisation) and magma mixing at different depths in both the mantle and continental crust (e.g., Aitcheson and Forrest, 1994; Davidson et al., 1991; Delacour et al., 2007; Gerbe and Thouret, 2004; Godoy et al., 2014; Hildreth and Moorbath, 1988; Mamani et al., 2010; Sørensen and Holm, 2008; Tepley et al., 2013; Thorpe et al., 1984; Thouret et al., 2005; Wilson, 1989).

Most current petrogenetic models for CVZ magmas consider that the primary calk-alkaline Plio-Quaternary magmas of southern Peru are derived from partial melting of a mantle wedge previously metasomatised by hydrous fluids released through dehydration of the subducted lithosphere, with subsequent crustal contamination during magma storage and ascent through the thick continental crust (65–70 km in southern Peru, Barazangi and Isacks, 1976). Some authors (e.g., Feeley and Davidson, 1994; Hildreth and Moorbath, 1988; Kay, 2002) assume that both mantle-derived and crustal magmas may have mixed and/or mingled at deep levels in a high-pressure MASH zone, thereby producing large volumes of contaminated andesitic magmas. Little to no sediments, however, are present on the subducting oceanic crust at the Peru–Chile trench (Thornburg and Kulm, 1987) and their subsequent role in crustal contamination of magmas can be precluded. Other studies suggest that tectonic shortening in the northern part of the CVZ resulted in significant crustal thickening, leading to a temperature increase in the lower crust, which promoted partial melting of local granulitic crust (Kay et al., 1999; Whitman et al., 1996). Additionally, low pressure assimilation and fractional crystallisation (AFC) processes, as well as magma mixing and/or crustal anatexis at higher crustal levels beneath large composite volcanic complexes may also impact the erupted magma compositions (e.g., Barreiro and Clark, 1984; Davidson and de Silva, 1995; Davidson et al., 1991; Godoy et al., 2014; Harmon et al., 1984; James, 1982; Tepley et al., 2013; Thorpe et al., 1984).

Such a combination of complex mechanisms that gradually modify the composition of different magma batches makes petrogenetic reconstructions difficult, yet a limited number of processes may have played a dominant role in the generation and evolution of these magmas, while others may be subordinate. Previous investigations, for example, suggested that the magma reservoir beneath El Misti volcano was several km^3 in volume and recurrently filled and homogenised prior to eruption (Ruprecht and Wörner, 2007). In addition, Tepley et al. (2013) proposed the existence of a temporary, shallow (~3 km deep), small-volume rhyolitic reservoir, most notably immediately

* Corresponding author at: Observatorio Vulcanológico del INGEMMET (Dirección de Geología Ambiental y Riesgo Geológico), Urb. Magisterial B-16, Yanahuara, Arequipa, Peru.
E-mail address: mrivera@ingemmet.gob.pe (M. Rivera).

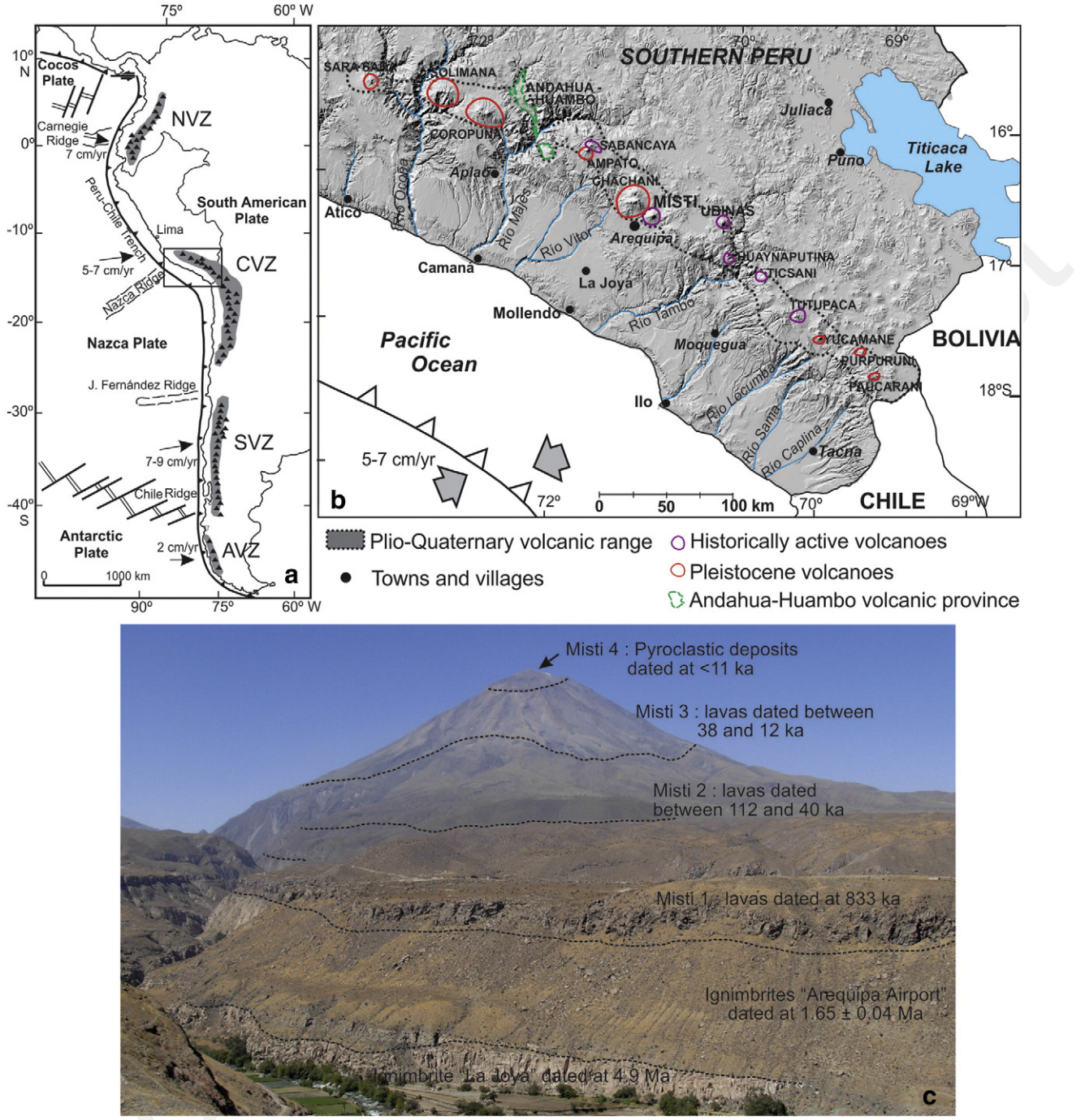

Fig. 1. (a) Location map of the South American volcanic zones: Northern (NVZ), Central (CVZ), Southern (SVZ) and Austral (AVZ), modified after Stern (2004). (b) Northernmost part of CVZ in southern Peru (modified after Thouret et al., 2005). El Misti volcano is located in the middle of the Plio-Quaternary volcanic range in southern Peru, 17 km NE of Arequipa city. (c) West flank of El Misti volcano (east bank of the Rio Chili canyon) where products of Misti 1 stratovolcano, Misti 2 and Misti 3 stratocones, and Misti 4 summit cone are exposed (after Thouret et al., 2001).

prior to the last plinian eruption of El Misti dated at 2070 ± 30 yr BP (Cobeñas et al., 2014). According to Kiebala (2008) the entire process of magma generation, ascent, storage, and eruption at El Misti occurs within cycles of 350 ka, translating into a long-term magma output rate of ~0.63 km^3/ka (Thouret et al., 2001).

In this paper we aim to identify the main mechanisms that control the composition of El Misti's erupted magmas, delineate the main sources of input into El Misti's magma chamber, and infer the petrogenetic processes involved during magma storage and ascent through the crust. Our approach is based on field geology as well as major and trace element systematics which, combined with Sr and Nd isotope data, are used for geochemical modelling. The results of the latter are combined with other evidence, such as the general geodynamic setting of the northern Central Andes, in order to propose a scenario for magma petrogenesis at El Misti that provides an example of the compositional variations observed in the northern CVZ.

2. Geological summary of El Misti volcano

2.1. Main structural features

Among the seven active volcanoes of southern Peru (Fig. 1b), El Misti (16°16′ S; 71°22′ W, 5822 m above sea level, asl.) is a major andesitic edifice located near the city of Arequipa (about 1,000,000 inhabitants)

in the northern CVZ. It straddles the western flank of the Western Cordillera, approximately 240 km east of the Peru-Chile trench and ~90 km above the top of the subducting Nazca plate (Syracuse et al., 2010). El Misti is a broadly conical, steep-sided, composite edifice with an asymmetrical shape controlled by the geometry of the high plateau and the western flank of the Western Cordillera. An outer summit crater is about 900 m in diameter and hosts an inner scoria ring truncated by a ~500 m-wide and 80 m-deep crater, which contains a small steaming lava plug (20 m high and 120 m wide).

El Misti is built upon older volcanic sequences emplaced during and after eruptions of the neighbouring Chachani volcano, which grew upon three prominent rhyodacitic ignimbrites, namely Rio Chili (ca. 13.3 Ma), La Joya (ca. 4.9 Ma) and Arequipa Airport (ca. 1.6 Ma) (Paquereau-Lebti et al., 2006, Fig. 1c). El Misti's growth essentially results from effusive activity that produced lava flows 20–60 m thick and up to 12 km long, with additional explosive eruptions of different magnitude (maximum Volcanic Explosivity Index [VEI] of 5, Harpel et al., 2011; Siebert et al., 2011), whose products have been partly eroded. The resulting pyroclastic and lahar deposits extend in the ring plain to the S and SW of the edifice, where they form gently dipping (<10°) fans upon which Arequipa is built.

2.2. Volcanological evolution

Previous geological studies of El Misti have noted two successive edifices (Legros, 2001; Suni, 1999; Thouret et al., 2001), consisting of one and three growth stages, respectively. The older edifice and stage, hereafter referred to as Misti 1, was built before 112 ka and consists of a 500 m-high stratocone that culminated at about 3500 m asl (Thouret et al., 2001). Products of the Misti 1 stage overlie volcaniclastic deposits from Chachani and the Miocene-Quaternary ignimbrite sequence (Paquereau-Lebti et al., 2006; Fig. 2). Either El Misti (Thouret et al., 2001) or Chachani (Ruprecht and Wörner, 2007) are possibly the source for lavas dated at 833 ± 6 ka, so until further evidence is forthcoming the earliest stage of El Misti's growth began between 833 ± 6 ka and 112 ± 6 ka. The resulting Misti 1 edifice consists of 20–60 m-thick blocky lava flows of andesitic to dacitic composition along with 4–12 m-thick andesitic scoria flow deposits. Sequences of such units exposed in walls of the Rio Chili canyon and at the southern and southwestern base of the present-day edifice reach a total thickness of about 400 m (Fig. 1c). The successions are covered in the south, southwest and west sides of the present-day cone by a 40–100 m-thick debris avalanche deposit, which formed when the southern flank of the Misti 1 edifice collapsed at ca. 112 ka (Thouret et al., 2001).

After 112 ka, the east and southeast slopes of the Misti 1 edifice were covered by a younger composite stratocone, which developed in three growth stages called Misti 2, Misti 3 and Misti 4 (Thouret et al., 2001, Figs. 1c and 2), as summarised below. During the Misti 2 stage (ca. 112–40 ka), three lithological sequences were emplaced. 1) A 500 m-thick sequence of 40–80 m-thick, blocky andesitic lavas and domes is dated between 112 and 70 ka (Thouret et al., 2001) and forms the basal and intermediate parts of El Misti´s present-day cone (Fig. 1c). On El Misti's lower south, southwest and northeast flanks such lavas are interbedded with block-and-ash and pumice-flow deposits. 2) A sequence of 10–20 m-thick andesitic breccias exposed 10 km south and southwest of the present-day crater has ages ranging

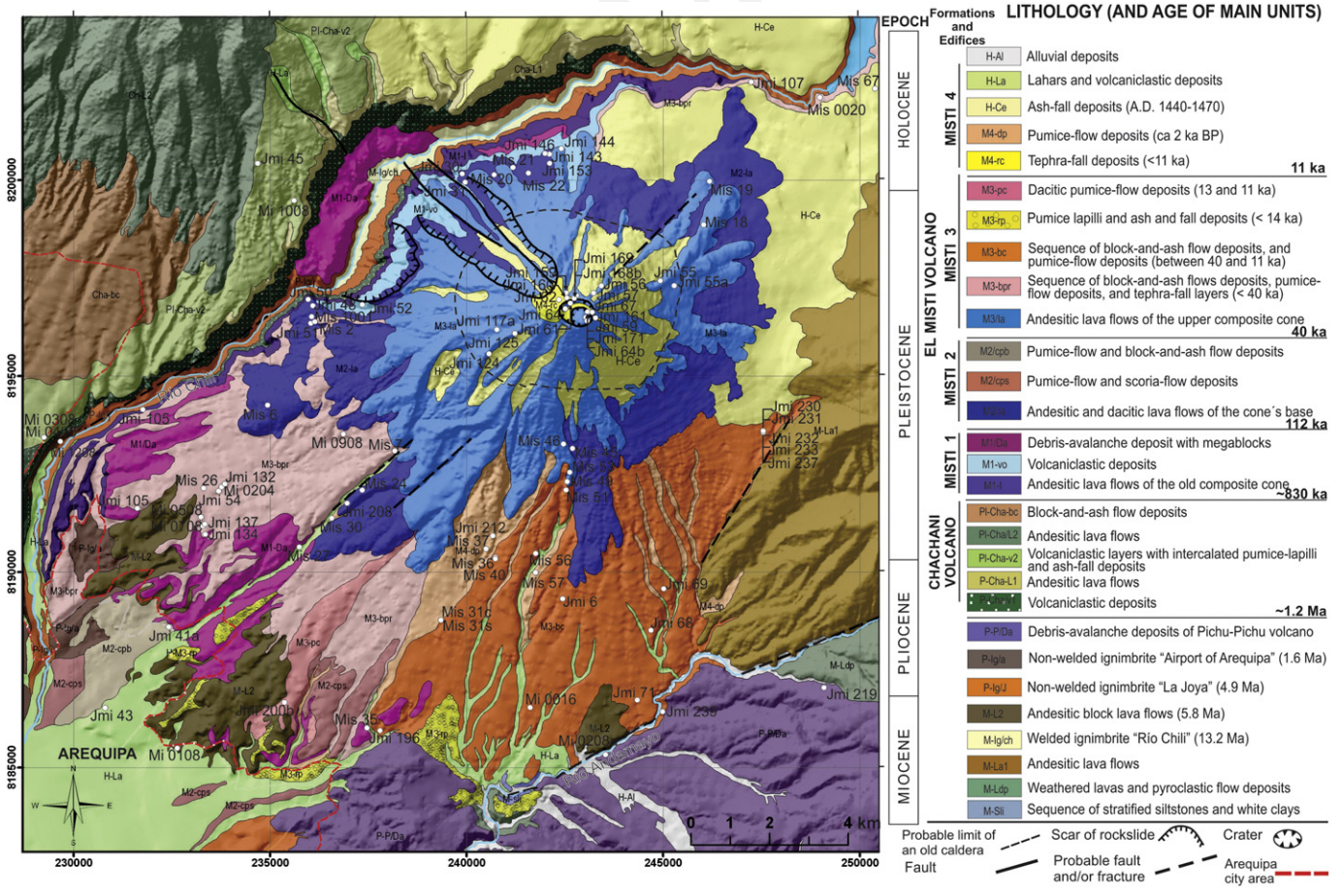

Fig. 2. Geological map of El Misti volcano (after Thouret et al., 2001) overlaid on a Digital Elevation Model. Lava and tephra samples analysed in this study are indicated by white dots.

Table 1
Textural and mineralogical characteristics of El Misti lavas. Mineral assemblages for each petrographic type are reported (*Pl* plagioclase, *Ol* olivine, *Opx* orthopyroxene, *Cpx* clinopyroxene, *Amp* amphibole, *Bt* biotite, *Mag* Magnetite, *Kfs* Alkali feldspar, *Ap* Apatite). Mineral abbreviations after Whitney and Evans (2010).

« Stage »	Misti 1	Misti 2	Misti 3	Misti 4
Rock type	Lavas			
Compositional range	Andesite (57.91–62.18 wt.% SiO_2)	Andesite (57.56–62.18 wt.% SiO_2)	Andesite (57.37–61.99 wt.% SiO_2)	
Phenocrysts % vol.	10–60	10–60	20–60	
Texture	Porphyritic	Porphyritic and microlitic, some time with groundmass intersertale	Porphyritic, microlitic	
Mineral assemblage	Pl ± Opx ± Cpx ± Amp + Mag	±Ol + Pl ± Px + Amp ± Bt + Mag	±Ol + Pl ± Px + Amp ± Bt + Mag ± Ap	
Vesicularity (%)	0–8	0–8	0–8	
Compositional range	Dacite (64.21–64.80 wt.% SiO_2)	Dacite (63.01–63.44 wt.% SiO_2)		
Phenocrysts % vol.	30–40	30–40		
Texture	Porphyritic	Porphyritic		
Mineral assemblage	Pl ± Opx + Amp + Mag	Pl ± Opx + Amp + Mag ± Ap		
Vesicularity (%)	0–4	2–4		
Rock type		Pumice and scoria belonging to pyroclastic flow and fall deposits		
Compositional range		Andesite (59.1–62.73 wt.% SiO_2)	Andesite (58.24–62.42 wt.% SiO_2)	Andesite (56.96–61.68 wt.% SiO_2)
Phenocrysts % vol.		10–20	5–50	5–50
Texture		Pl + Opx + Amp + Mag	Pl ± Opx + Cpx + Amp + Mag	±Ol + Pl ± Opx + Cpx + Amp + Mag
Mineral assemblage		Porphyritic	Porphyritic and microlitic, some time with groundmass intersertale; vitroclastic	Porphyritic and microlitic, some time with groundmass intersertale
Vesicularity (%)		10–50	10–40	10–60
Compositional range			Dacite (63.38–65.17 wt.% SiO_2)	Dacite (63.02–63.15 wt.% SiO_2)
Phenocrysts % vol.			20–40	20–25
Texture			Porphyritic, vitroclastic	Porphyritic
Mineral assemblage			Pl ± Opx + Amp ± Bt + Mag ± Ap	Pl + Opx + Amp + Mag
Vesicularity (%)			5–40	30–40
Compositional range			Rhyolite (72.35–73.59 wt.% SiO_2)	
Phenocrysts % vol.			10–30	
Texture			Porphyritic, vitroclastic	
Mineral assemblage			Pl + Kfs + Bt + Mag ± Ap	
Vesicularity (%)			30–40	

from 70 to 50 ka. Such breccias are part of a debris-avalanche deposit from the collapse of El Misti's south flank. 3) A sequence of indurated 12–25 m-thick andesitic to dacitic pumice-flow deposits was emplaced from 50 to 40 ka and crops out at the south and southeast base of the volcano. Thouret et al. (2001) correlate these deposits to the formation of a summit caldera or a cluster of craters.

Misti 3 stage (38–11 ka) consists of four lithological sequences. (1) The lowest sequence consists of lavas of the upper cone (from 4400 to 5600 m asl.) (Fig. 2), andesitic to rhyolitic pumice-flow deposits dated at 34–31 ka (Thouret et al., 2001), and dacitic to rhyolitic tephra-fall deposits. (2) A diverse sequence of dacitic pumice-flow deposits and andesitic block-and-ash-flow deposits is interbedded with pumice-fall layers emplaced between 30 ka and 25 ka. Such deposits have a composite thickness of 80–100 m and crop out 6–10 km from the vent on the south flank of El Misti in Huarangal, Honda, and Grande ravines (Fig. 2). (3) Between 25 and 20 ka at least five 5–20 m-thick andesitic block-and-ash flow deposits with intercalated andesitic tephra-fall layers were emplaced. Lahar deposits and additional tephra-fall layers are intercalated with the block-and-ash flow deposits at the top of the sequence. Such deposits crop out at the southern base of the volcano in Honda and Grande ravines. (4) The uppermost sequence (14–11 ka) includes two voluminous (~1 km^3) dacitic pumice-flow deposits interbedded with two distinctive pumice-fall layers and two thin, partly cross-bedded surge deposits. The pyroclastic density currents (PDCs) deposits are exposed 12 km from the summit to the south and southwest, in the Los Gráficos and San Luis areas, where they are 6–8 m-thick. These conspicuous pumice-flow deposits, in addition to morphological and geophysical evidence, suggest a now-buried ~2 km-diameter caldera at the summit of the Misti 3 cone (about 5400 m asl.).

Finally, the youngest (<11 ka) Misti 4 stage comprises a sequence of at least ten thin pumice lapilli and ash-fall and flow layers resulting from moderate-sized Plinian, Subplinian and Vulcanian eruptions (Fig. 2). At about 6–8 km away from the source, these tephra deposits crop out as 5–35 cm-thick layers. The most recent ca. 2 ka BP Plinian VEI-5 eruption produced 1.4 km^3 of tephra-fall deposits (~20 cm thick in Arequipa's city center), 0.01 km^3 of PDC deposits (Harpel et al., 2011), and seemingly resulted in the formation of the current 900 m-wide summit crater (Fig. 2). Other minor explosive events occurred in late pre-Columbian times, most notably in the fifteenth century (AD 1440–1470, VEI 2), with deposition of andesitic tephra and formation of a lava plug inside the present-day inner crater. El Misti's historical activity consists of occasional phreatic and fumarolic events with sporadic small-volume lahars (Chavéz Chavéz, 1992; Delaite et al., 2005; Suni, 1999; Thouret et al., 2001).

3. Sample collection and preparation, and analytical methods

3.1. Field sampling and sample preparation

Geologic mapping, stratigraphic studies and sampling occurred between 2005 and 2008. We collected 142 samples that are representative of all of the edifice's major pyroclastic and lavaflow units. Thin sections of all samples were prepared for petrographic studies and electron microprobe analysis.

3.2. Analytical methods

We selected 123 fresh samples for major and trace elements analyses and 10 samples for Nd and Sr isotopic analyses. A description of the principal petrographic characteristics of the sampled volcanic units is given in Table 1, while the analytical procedures are summarised below.

3.2.1. Mineral analyses

The mineral analyses were obtained using a CAMECA SX-100 electron microprobe at the Laboratoire Magmas et Volcans (Université Clermont Auvergne, Clermont-Ferrand, France). Operating conditions were 15 kV accelerating voltage, 10 nA beam current, and 10 s counting time. The estimated uncertainty for a single analysis is about 1% when the element concentration is higher than 10%, whereas for element concentrations lower than 10% uncertainty is 2–5%. Composition data for phenocrysts from each volcanic unit are presented in Supplementary Electronic Material (SEM 1).

3.2.2. Major and trace element analyses

Major element concentrations of 10 whole-rock samples were determined by ICP-AES and trace elements by ICP-MS on 20 g aliquots of rock powder at ACME Laboratories in Vancouver, Canada. Major and trace element abundances were determined on 0.1 g samples following a lithium metaborate–tetraborate fusion and dilute nitric acid digestion. Loss on ignition (LOI) was determined by weight difference after ignition at 1000 °C. Analytical precisions vary from 0.1% to 0.04% for major elements, from 0.1 to 0.5 ppm for trace elements, and from 0.01 to 0.5 ppm for rare earth elements.

Six analyses of the standard SO-18 were performed during the same analytical session as our samples. They are accurate to <1% relative for all elements, and are consistent with the expected values for this standard. Duplicate measurements on samples of an andesite and a dacite yielded an estimate of the total reproducibility of these analyses. The results demonstrate that the reproducibility is better than 4% for major elements and generally better than 8% for trace elements, except for Tm (8–10%), Zr and Hf (12–14%). Five blanks display measured values typically under detection limits for all major and trace elements. A detailed description of the procedure and additional information about methods and analytical reproductibility can be also found at http://www.acmelab.com.

Major and trace element concentrations of an additional 113 whole-rock samples from El Misti volcano were analysed at the Laboratoire Domaines Océaniques, Université de Bretagne Occidentale (Brest, France). Chemical analyses were obtained from inductively coupled plasma-atomic emission spectroscopy (ICP-AES), except for Rb, which was determined by flame AES (Cotten et al., 1995). Relative standard deviations are 1% for SiO_2 and <2% for the other major elements, except for low concentrations (<0.50%) for which the absolute standard deviation is 0.01%. For trace elements, the relative standard deviation is ca. 5% except for Er (ca. 20%). Calibrations were made using international standards JB2, BEN, ACE, WS-E, PM-S as well as specific reference samples. To determine interlaboratory consistency, some of our samples were analysed at both laboratories yielding results within analytical uncertainties for the ICP-AES and ICP-MS methods. As such, we report the entire composite data set here. All analyses were recalculated on an anhydrous basis with iron expressed as $Fe_2O_3t = Fe_2O_3 + 1.111$ FeO. Results of the analyses are given in Table 2 and Supplementary Electronic Material (SEM 2).

3.2.3. Sr–Nd analyses

Sr- and Nd-isotope analyses of 10 samples from El Misti lavas were performed at the Laboratoire Magmas et Volcans (Université Clermont Auvergne; Clermont-Ferrand, France) on whole-rock powders, which were dissolved using an $HF/HNO_3/HClO_4$ mixture. Sr and Nd were separated by ion-exchange chromatography according to the procedures described in Pin et al. (1994) and Pin and Bassin (1992). $^{87}Sr/^{86}Sr$ and $^{143}Nd/^{144}Nd$ isotopic ratios were determined using either a VG Isomass 54E multicollector mass spectrometer or a Finnigan TRITON. During the period of measurements, SRM-987 and AMES Rennes standards gave $^{87}Sr/^{86}Sr = 0.710239 \pm 0.00002$ (2σ, n = 4) and $^{143}Nd/^{144}Nd = 0.5119651 \pm 0.000015$ (2σ, n = 4). Six Sr–Nd isotopic ratios published by Mamani et al. (2010) are also considered in

Table 2
Selected whole-rocks analyses of Misti volcano: major (wt.%) and trace elements (ppm) and isotopicratios.

Unit	Misti 1				Misti 2						Misti 3
Sample	JMI-30	JMI-68	JMI-69	JMI-107	MIS-36	JMI-146	JMI-55	JMI-55a	JMI-153	MI-1208	MIS-0204
Location	NW flank, río Chili	NW flank, río Chili	Q. Cangallo	NW flank, río Chili	Q. Guarangal	NW flank	NE flank	NE flank	NW flank	NW flank, río Chili	Q. Pastores
Rock type	Lava flow	Lava flow	Lava flow	Scoria	Lava flow	Lava flow	Lava flow	Lava flow	Lava flow	Pumice of flow	Scoria
Analytical Technique	ICP-AES	ICP-AES	ICP-AES	ICP-AES	ICP-AES	ICP-AES	ICP-AES	ICP-AES	ICP-AES	XRF/ICP-MS	XRF/ICP-MS
Major elements (wt%)											
SiO2	58.20	60.15	60.30	59.00	61.8	59.70	60.40	58.80	57.50	58.43	57.70
TiO2	0.80	0.78	0.75	0.89	0.62	0.70	0.79	0.86	0.87	0.79	0.89
Al2O3	17.58	17.50	17.50	17.00	17.25	17.60	17.50	17.50	17.30	17.50	17.00
Fe2O3t	6.72	6.16	5.98	6.56	5.45	6.55	6.08	6.49	6.91	6.59	6.62
MnO	0.10	0.10	0.10	0.09	0.10	0.11	0.09	0.09	0.10	0.10	0.10
MgO	3.14	2.67	2.53	3.22	2.38	2.64	2.73	3.14	3.63	2.96	3.33
CaO	5.97	5.34	5.26	5.60	5.16	5.75	5.48	6.04	6.30	5.83	5.95
Na2O	4.24	4.39	4.48	4.38	4.14	4.15	4.28	4.40	4.55	4.17	4.07
K2O	2.06	2.30	2.27	2.25	2.25	2.03	2.32	2.00	2.40	2.20	2.08
P2O5	0.25	0.26	0.26	0.30	0.24	0.29	0.24	0.26	0.33	0.30	0.30
LOI	0.86	0.28	0.40	0.62	0.46	0.18	0.10	0.37	0.23	0.8	
Total	99.92	99.93	99.83	99.91	99.85	99.70	100.01	99.95	100.12	99.67	98.04
Trace elements (ppm)											
Rb	39	41	43	45	43	39	50	34	44	40.0	34
Sr	824	830	825	840	760	813	810	850	1035	810	868
Ba	935	1040	1030	1030	1075	1035	1035	925	1200	953	962
Sc	12.8	10.5	9.6	11.6	10.0	11.1	11.4	11.5	15.2	11.1	16.1
V	160	135	127	150	110	127	148	165	165	140	150
Cr	23	25	23	65	25	21	26	72	53		67
Co	20	18	17	42	15	18	19	21	21	19	20
Ni	27	27	24	38	17	18	28	40	42	21	34
Y	13.8	12.5	12.3	13.2	12.1	13.8	11.8	11.6	15.0	13.5	14.1
Zr	147	169	160	180	155	155	162	148	186	153	170
Nb	5.2	5.6	5.5	6.2	5.9	6.0	5.7	5.4	6.4	5.4	5.0
La	25	27	28	35	29	28	29	25	48	26	27
Ce	48	55	55	71	54	57	56	50	91	53	51
Nd	23	27	28	30	24	26	25	24	39	27	22
Sm	4.3	4.6	4.6	5.5		4.5	4.4	4.6	5.8	4.5	4.2
Eu	1.2	1.3	1.2	1.4	1.1	1.2	1.2	1.3	1.5	1.3	1.4
Gd	3.9	3.4	3.3	4.5		3.4	3.3	3.3	4.1	3.6	3.8
Dy	2.5	2.3	2.3	2.6	2.2	2.5	2.2	2.2	2.6	2.6	2.3
Er	1.5	1.3	1.5	1.3	1.3	1.3	1.3	1.3	1.3	1.4	1.2
Yb	1.17	1.07	1.04	1.01	1.05	1.13	0.98	0.90	1.16	1.19	1.20
Th	2.0	2.5	2.8	2.9	2.2	2.5	3.5	1.8	3.2	2.2	2.5
87Sr/86Sr									0.70715	0.70750	
±2σ									0.000010	0.000008	
εSr									37.56	42.58	
143Nd/144Nd									0.51228	0.512165	
±2σ									6E-06	0.000006	
εNd									-7.04	-9.23	

addition to our data. Selected whole-rock analyses and all isotopic data are presented in Table 2.

4. Characterisation of El Misti volcanic rocks

4.1. Petrography and mineral compositions

Mineral assemblages and textures are fairly similar throughout El Misti's entire eruptive history (Table 1). The lavas are andesitic (~86%), dacitic (~11%) and rhyolitic (~3%) in composition with andesites dominating our sample collection. All andesites have an assemblage of plagioclase (Pl), orthopyroxene (Opx), clinopyroxene (Cpx), amphibole (Amp) and magnetite (Mag) together with rare olivine and apatite. While such mineral phases are ubiquitous, their relative proportions are quite variable. The dacites host a Pl + Amp + Cpx + Mag assemblage whereas the rhyolites lack pyroxene and amphibole and, instead, contain Pl + Kfs (Alkali feldspar) + Bt (Biotite) + Mag (Table 1). Most lava and pyroclastic samples exhibit porphyritic textures with intersertal or microlitic groundmass. Phenocrysts represent about 15 vol.% and are generally 300–800 μm, but rarely can be more than 1.5 mm in length. A few samples (<10%) display subaphyric to slightly porphyritic textures. Some pumice clasts from the ca. 2 ka BP eruption (Misti 4) are texturally heterogeneous with banded layers of contrasting grey to brown. When considering the entire El Misti petrological suite, plagioclase is by far the most abundant mineral phase, followed in abundance by amphibole and pyroxene, while olivine is extremely rare and only occurs in some andesites. Biotite is observed only in dacitic and rhyolitic samples while alkali feldspar is present in most rhyolites and some andesites. Fe-Ti oxides are reported in all samples, but apatite occurs only as an occasional accessory phase.

4.1.1. Feldspars

Plagioclase phenocrysts are abundant (10–25 vol.%) in all El Misti rocks (Table 1). In Misti 1, 2 and 4 andesites, the anorthite content in plagioclase phenocrysts ranges from An_{38} to An_{78}, reaching a maximum of An_{86} in Misti 3 andesites (SEM 1). The composition of plagioclase microlites varies within a similar range from An_{38} to An_{84}. In dacites and rhyolites, the plagioclase is mainly andesine ($An_{31–47}$). Normal zoning is present in some phenocrysts (e.g., andesite JMI-171: $An_{68–53}$; dacite JMI-143: $An_{73–58}$ and rhyolite MI0508: $An_{38–29}$) while reverse zoning is scarce (e.g., andesite JMI-66: $An_{46–52}$; dacites JMI 200B: $An_{42–51}$). Dusty concentric zones in both cores and rims are present

						Misti 4				
MI-0508	MI-0208A	MI-0408	MI-0708	JMI-66	JMI-200B	JMI-64b	MIS0020	JMI-45	JMI-161	JMI-168B
Q. Pastores	Chiguata	Cayma	Q. Pastores	Summit, northern flank	Q. Huarangal	Top of the volcano	Aguada Blanca dam	Road to Chachani	Summit, WNW flank	Top of the volcano
Pumice fall	Pumice fall	Pumice fall	Pumice	Lava flow	Pumice	Juvenile block	Scoria flow	Pumice fall	Scoria	Bomb
XRF/ICP-MS	XRF/ICP-MS	XRF/ICP-MS	XRF/ICP-MS	ICP-AES	ICP-AES	ICP-AES	XRF/ICP-MS	ICP-AES	ICP-AES	ICP-AES
69.61	70.67	69.35	62.86	61.00	62.60	59.60	58.00	59.70	59.50	59.80
0.16	0.16	0.16	0.62	0.79	0.61	0.87	0.79	0.66	0.82	0.87
14.35	14.66	14.53	14.91	17.20	16.20	17.05	17.60	17.25	17.00	17.05
1.44	1.34	1.46	5.39	6.00	5.06	6.45	6.54	5.46	6.45	6.43
0.09	0.09	0.09	0.10	0.09	0.09	0.09	0.10	0.10	0.09	0.09
0.38	0.42	0.45	2.26	2.64	2.32	3.12	3.09	2.14	3.00	3.05
1.27	1.40	1.52	3.61	5.17	4.55	5.41	6.12	4.89	5.90	5.12
3.96	3.80	3.86	3.60	4.39	3.85	4.24	4.22	4.09	4.21	4.38
3.49	3.89	3.63	2.87	2.57	2.58	2.55	2.06	2.33	1.99	2.54
0.13	0.11	0.15	0.24	0.29	0.21	0.30	0.25	0.25	0.31	0.30
4.9	3.3	4.6	3.3	-0.10	1.76	0.14	1.18	2.55	0.44	0.04
99.78	99.84	99.80	99.76	100.04	99.83	99.82	99.78	99.63	99.71	99.67
71	72	74	56	52	52	53	44	48	41	52
333	377	386	518	870	697	925	788	774	855	927
1151	1199	1205	987	1170	1090	1140	915	1112	985	1085
2.2	2.1	2.3	9.4	10.0	8.7	13.2	9.2	8.3	11.3	13.1
18	8	13	101	128	100	150	144	104	135	150
	6	5		49	34	73	19	17	31	66
0.9	0.5	0.2	13	17	19	27	42	19	20	19
4	2	6	20	29	21	42	17	16	28	37
9.4	9.5	11.3	12.7	11.5	11.3	12.6	15.0	12.8	11.0	12.4
119	131	121	179	184	110	185	158	182	150	195
7.7	8.5	8.7	7.6	6.8	6.1	6.0	7.0	6.5	5.9	6.4
25	27	27	31	38	32	39	33	33	25	39
49	52	52	62	71	56	75	68	63	47	73
18	21	21	28	33	25	35	31	27	25	32
2.8	3.0	3.4	4.4	5.2	4.6	5.9	5.7	4.6	4.1	5.6
0.7	0.7	0.8	1.0	1.3	1.1	1.4	1.3	1.2	1.2	1.3
2.0	2.1	2.3	3.3	3.4	3.4	3.5	5.0	3.3	3.4	3.8
1.7	1.7	2.1	2.3	2.3	2.1	2.4	3.3	2.4	2.1	2.4
0.8	0.9	1.0	1.2	1.3	1.0	1.4	1.8	1.3	1.0	1.1
0.86	0.87	0.95	1.08	0.93	0.97	1.06	1.43	1.10	0.94	1.03
3.8	4.6	4.8	3.8	3.6	3.7	4.3	3.4	3.4	2.2	4.2
	0.70882	0.70878	0.70828	0.70774	0.70795	0.70795	0.70746	0.70757		
	0.00001	0.000008	0.000006	8E-06	8E-06	8E-06	9E-06	0.00001		
	61.25	60.78	53.68	46.05	48.93	48.90	42.00	43.58		
	0.511986	0.511983	0.512048	0.51213	0.51205	0.51213	0.51213	0.512157		
	0.000006	0.000008	0.000006	8E-06	8E-06	4E-06	4E-06	6E-06		
	-12.72	-12.78	-11.51	-9.97	-11.57	-9.93	-9.99	-9.38		

in <10% of the phenocrysts. Sieve textures reflect dissolution features linked to a perturbation during crystal growth and are commonly attributed to episodes of magma mixing (Coombs et al., 2000; Kawamoto, 1992). The alkali feldspars are sanidine ($Or_{50–53}$) in Misti 4 andesites and anorthose ($Or_{26–32}$) in Misti 3 rhyolites. In the latter silicic magmas, crystallisation of alkali feldspar started after the completion of plagioclase crystallisation (Rivera, 2010).

4.1.2. Clinopyroxene

Clinopyroxene occurs as euhedral to subhedral phenocrysts (0–15 vol.%) as well as microlites in andesites and dacites (Table 1). Such clinopyroxenes have a relatively stable compositional range from diopside to magnesian augite ($Wo_{39–50}$, $En_{40–50}$, $Fs_{7–16}$) with Mg# (Mg# = molecular Mg/(Mg + Fe^{2+})* 100; Morimoto et al., 1988) from 74 to 88 (SEM 1). Normal zoning (e.g., JMI-31: Mg#81-79; JMI-48: Mg#79-77; JMI-159: Mg#88-83) is typical while reversed zoning (e.g., JMI-55a: Mg#71-80; JMI-66: Mg#74-86) is also observed. The relationship of CaO vs. Mg# indicates that clinopyroxene remained stable throughout the entire magmatic history of the volcano. However, during each eruptive stage the pyroxene composition evolved towards a more Fe-rich composition through the course of magma differentiation. In addition, the presence of diopside and Ca-rich augite indicates that the differentiation process took place under high fO_2 (Wilson, 1989).

4.1.3. Orthopyroxene

Euhedral and subhedral orthopyroxenes are present as phenocrysts and microlites (0–15 vol.%) in most andesites and some dacites (Table 1). They display a compositional range from En_{64} to En_{83} (SEM 1). Zoning in such orthopyroxenes is usually normal (e.g., JMI-50: Mg# 73-73; JMI-171: Mg# 83-79; JMI-164bis: Mg# 82-79), though rare reversely zoned examples are present (e.g., JMI-55a: Mg# 70-79; JMI-61: Mg# 73-82).

4.1.4. Amphibole

Amphibole is ubiquitous in andesitic and dacitic lavas and pyroclasts (Table 1). Their compositions are pargasite and tschermakite (Fig. 3) (Leake et al., 1997), depending on the amount of alkali elements (Na + K) in site A with a threshold of (Na + K) = 0.50 atoms per formula unit (a.p.f.u.). Such amphiboles in andesites and dacites have a Mg# from 70 to 94 and from 67 to 90, respectively. Normal zoning

prevails (e.g., JMi-52: Mg# 86-81; JMi-45: Mg# 91-84; Mis0017: Mg# 84-77) while reverse zoning is scarce (e.g., JMi-143: Mg# 81-87; JMi-117: Mg# 75-80; Mi1508: Mg# 76-81) (SEM 1). Amphibole typically occurs in magmas with more than 5 wt.% water and its crystallisation is promoted by high H_2O pressure that commonly characterises continental arc settings (Davidson et al., 1991).

In some lava, scoria and block samples, amphibole crystals are rimmed by opaque mineral coronaes, in which complete replacement (pseudomorphosis) of amphibole is achieved through crystallisation of Fe-Ti oxide and pyroxene aggregates (black-type alteration). Where the original morphology of the pseudomorphosed amphiboles is preserved, analyses of the coronaes reveal a composition of a Fe-Ti oxide or pyroxene. This type of substitution may result from pre-eruptive magma mixing (isobaric heating) or oxidation when the magma is erupted through isothermal decompression (Ridolfi et al., 2010; Rutherford and Hill, 1993).

4.1.5. Biotite

Biotite crystals only occur in a few pyroclastic dacites and rhyolites of Misti 3, as well as in rare andesite lavas of Misti 2 and 3, and their compositions are reported in SEM 1. Such crystals have relatively low Mg#s (54 to 58) within a narrow range when compared with associated amphibole (6 to 94), which indicates that iron is more efficiently fractionated by biotite than amphibole. In addition, the Misti biotite is relatively Al-rich (Al^{IV} 1.1–2.1 a.p.f.u.) and TiO_2-poor (Ti 0.12–0.25 cations p.f.u.) suggesting lower crystallisation temperatures (Patiño Douce, 1993).

4.1.6. Olivine

Olivine occurs only in mafic andesites and when present is scarce, never exceeding 2 vol.%. In thin section, the olivines are subhedral to anhedral with sizes smaller than 400 μm. Misti 2 olivine has a Forsterite composition of Fo_{76-80} while Misti 3 olivine has a slightly lower magnesium content (Fo_{70-78}) (SEM 1). Subtle normal zoning is present in olivine from both Misti 2 and 3. When compared with olivine from primitive arc magmas (>Fo_{80}, Tamura et al., 2000; Ruscitto et al., 2011; Sorbadère et al., 2013) the relatively low Fo content of the El Misti olivine (Fo_{70-80}) provides evidence against a pure, primary, mantled-derived origin for El Misti rocks.

4.1.7. Fe-Ti oxides

Fe-Ti oxides (with sizes up to 50 μm) are present in the groundmass or as inclusions within pyroxene, biotite, amphibole, and some plagioclase phenocrysts. All studied samples contain titano-magnetite, but only a few samples from Misti 3 contain ilmenite (SEM 1). This latter mineral phase is only present as euhedral microphenocrysts in high-silica andesites and dacites.

4.1.8. Accessory minerals

Quartz appears as spherical microphenocrysts in the silica-rich samples (SiO_2 > 64 wt.%) or as small grains in the groundmass. Apatite is found as inclusions in almost all other mineral phases (pyroxene, amphibole, biotite, and plagioclase).

4.2. Main geochemical characteristics

All analysed samples plot in the high-K calc-alkaline field of Peccerillo and Taylor (1976) (Fig. 4), which is typical of modern continental arcs. Despite the wide compositional range between andesites and rhyolites at El Misti, most samples are andesites and dacites, a common feature of the CVZ volcanic rocks (e.g., Delacour et al., 2007; Gerbe and Thouret, 2004; Mamani et al., 2010; Rivera et al., 2014; Sørensen and Holm, 2008; Thouret et al., 2005; Wilson, 1989). However, the andesite/dacite ratio decreases with time from essentially andesites in Misti 1 to increasing amounts of dacites and eventually rhyolites in Misti 3. Basalt and basaltic andesite compositions are absent. When plotted in Harker diagrams (Fig. 4), the andesites and dacites align along a single continuous trend, whereas Misti 3 rhyolites are separated from other lavas by a compositional gap between 66 and 73 wt.% SiO_2. We surmise that this gap is not due to a sampling bias, but rather reflects a real compositional hiatus at the scale of the entire volcano.

In Harker diagrams (Fig. 4), all major elements except K_2O are negatively correlated to SiO_2. Similarly, transition elements (e.g., Ni, V) and Sr, Sm and possibly Yb are negatively correlated to SiO_2. Conversely, Rb, Nb, Ba and to some extent La show a positive correlation. In some diagrams, for instance Ni vs. SiO_2, the trends are not linear but rather follow curved or broken trends, a feature that precludes magma mixing as one of the prevailing magmatic processes. In contrast, Rb behaves as an incompatible element whereas Cr and V are strongly compatible. In a log (compatible element) vs. log (incompatible element) plot, differentiated liquids produced by partial melting show a sub-horizontal trend whereas fractional crystallisation would rise to a sub-vertical trend (Cocherie, 1986; Janoušek et al., 2015; Martin, 1987; Wilson, 1989). Plotting log(V) vs. log(Rb) and log(Cr) vs. log(Rb) yields clearly defined sub-vertical trends (Fig. 5) suggesting that fractional crystallisation is the main process driving magma differentiation.

However, detailed inspection of our data set reveals a more complicated magmatic evolution. Indeed, Ba, Th and to a lesser extent K_2O, Na_2O, Rb and Sr contents show a high variability in andesites as well as in some dacites, which cannot be attributed to total analytical uncertainty (see the Analytical methods Section 3.2.2).

Multi-element diagrams normalised to primitive mantle (Sun and McDonough, 1989) suggest that El Misti lavas are chemically typical of continental arc magmas (Fig. 6). Such lavas are enriched (~100 times) in large-ion lithophile elements (LILE; e.g. Rb, Ba, K) and display a marked negative anomaly in Nb and Ti (notably in Misti 3 rhyolites) compared to the primitive mantle. Whereas, heavy rare earth element (HREE; e.g. Yb) contents remain low and are associated with relatively high Sr contents and a small positive Sr anomaly (Fig. 6).

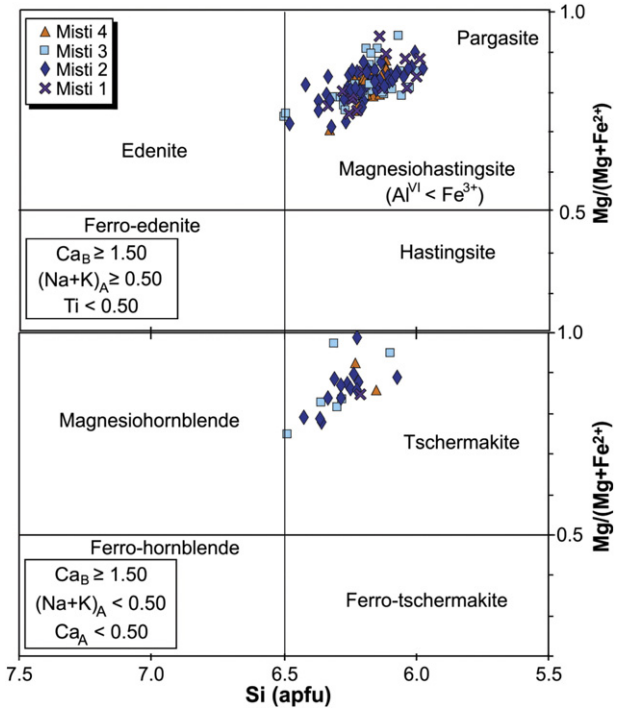

Fig. 3. Mg/(Mg + Fe^{2+}) vs. Si (a.p.f.u., atoms per formula unit) diagram for calcic amphibole (nomenclature after Leake et al., 1997) showing that El Misti's amphiboles are pargasite (with: $Ca_B \geq 1.50$, $(Na + K)_A < 0.50$ and $Ti < 0.5$) and tschermakite (with: $Ca_B \geq 1.50$, $(Na + K)_A \geq 0.50$ and $Ca_A < 0.5$).

The REE (Rare Earth Elements) patterns normalised to chondrites are LREE (light-REE)-rich ($92.9 < La_N < 202.5$) and low in HREE ($5.3 < Yb_N < 8.9$), which results in fractionated patterns ($12.4 < (La/Yb)_N < 30.3$). When compared to common calc-alkaline magmas from oceanic arcs well-away from any continental influence (e.g. Vanuatu; Monzier et al., 1997), El Misti lavas are significantly lower in HREE. These REE patterns are also characterised by the lack of significant Eu anomalies, which could be explained by processes such as: (1) crystallisation under high fO_2 conditions preferentially involving Eu^{3+} (Davidson et al., 1990); (2) high water pressure leading to partial inhibition of plagioclase crystallisation (Sisson and Grove, 1993), and; (3) the effect of plagioclase crystallisation ($Kd^{Plag/liq}_{Sm/Eu}<1$) is reduced or hampered through concomitant crystallisation of amphibole ($Kd^{Hbd/liq}_{Sm/Eu}>1$) (Martin, 1987).

4.3. Isotopic data

Table 2 summarises Nd and Sr isotopic analyses of 10 rock samples. When compared with other primitive calk-alkaline magmas from the CVZ, El Misti lavas yield the highest $^{87}Sr/^{86}Sr$ (0.70715–0.70882) and lowest $^{143}Nd/^{144}Nd$ (0.511983–0.512277) ratios yet published (Fig. 7a). Plotting $^{143}Nd/^{144}Nd$ vs. $^{87}Sr/^{86}Sr$ (Fig. 7a) highlights that most El Misti rocks are outliers with respect to the previously defined field for CVZ lavas (Davidson et al., 1991). Such behaviour suggests that El Misti magmas are the most crustally-contaminated of all the CVZ magmas. This hypothesis is corroborated by a positive correlation of $^{87}Sr/^{86}Sr$ with SiO_2 (Fig. 7b) and a negative correlation of $^{143}Nd/^{144}Nd$ with SiO_2. We emphasise, however, that both trends are controlled by Misti 3 rhyolites.

5. Discussion

5.1. Change in magma composition through time

Plotting major and trace element compositions against the stratigraphic succession and age of the erupted products (Fig. 8) suggests that magma composition remains fairly constant through time, varying in a narrow range of silica content ($57 \text{ wt.\%} < SiO_2 < 65 \text{ wt.\%}$). During the

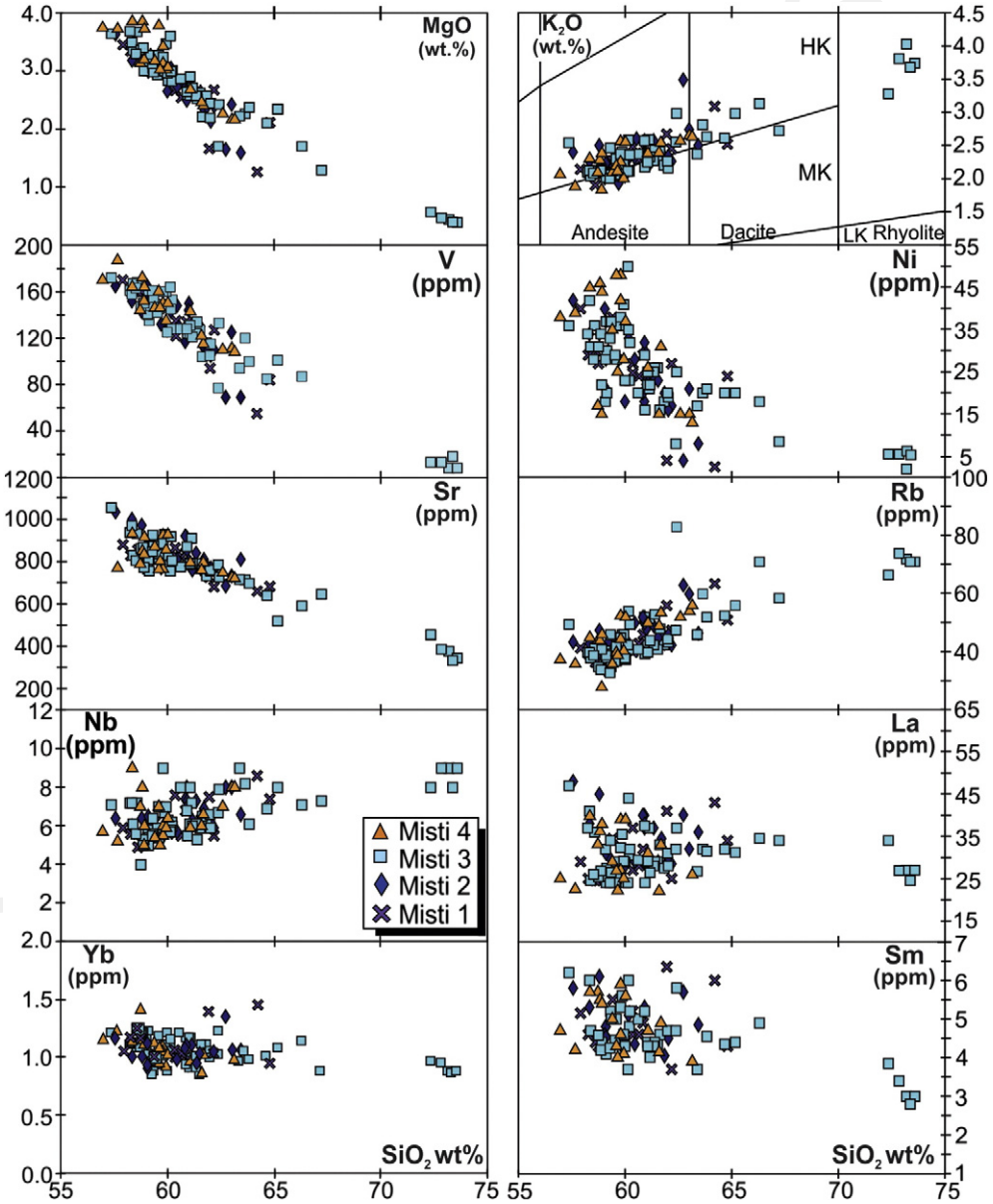

Fig. 4. Major oxides and trace element variation diagrams (Harker, 1909). Petrographic fields after Peccerillo and Taylor (1976) in the K_2O vs. SiO_2 diagram. All major elements (except K_2O) and transition elements (e.g., Ni, V), Sr, Sm and possibly Yb are negatively correlated with SiO_2, while K_2O, Rb, Ba, Nb, and to some extent La show a positive correlation.

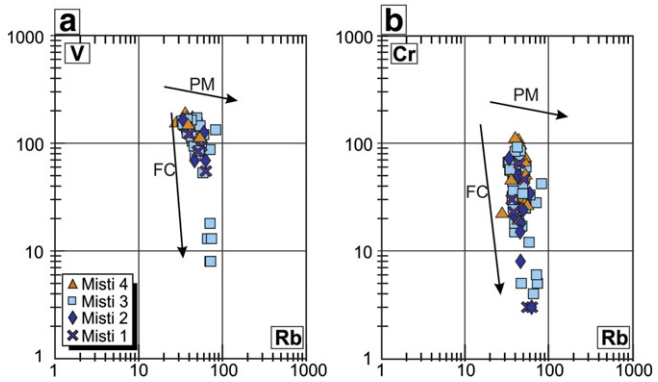

Fig. 5. Models of fractional crystallisation for El Misti magmas. (a) Log (V) vs. Log (Rb) and (b) Log (Cr) vs. Log (Rb) diagrams. FC fractional crystallisation; PM partial melting.

Misti 3 stage, however, the magma SiO_2 content reached values as high as 74 wt.%. Conversely, MgO content displays the opposite trend and is marked by low contents during the Misti 3 stage. Trace element contents (Rb) and ratios (Sr/Y and Rb/Zr) in conjunction with $^{87}Sr/^{86}Sr$ ratios (Fig. 8) all show similar patterns of temporal evolution delineated by a narrow range of variations during Misti stages 1, 2 and 4 and significant deviations during a brief episode within Misti 3. Pumice-fall and PDC deposits characterised by high-silica and low-Mg dacite and rhyolite were emplaced during stage 3, ca. 34–31 ka ago. This episode coincides with high $^{87}Sr/^{86}Sr$ and low $^{143}Nd/^{144}Nd$ ratios, which support the hypothesis that the main contamination event occurred between ca. 34 and 31 ka. A slightly more extended compositional range is also observed between 70 and 40 ka, although no rhyolites were erupted within that time interval (Legendre, 1999; Ruprecht and Wörner, 2007; Thouret et al., 2001).

5.2. Potential sources of El Misti magmas

5.2.1. Mantle source

Previous studies (Davidson et al., 1991; Lefèvre, 1979; Legendre, 1999; Mamani et al., 2010; Ruprecht and Wörner, 2007) suggest that El Misti magmas result from partial melting of a mantle wedge peridotite that was previously metasomatised by fluids released by dehydration of the subducting slab. SiO_2 and MgO contents as well as Sr and Nd isotope signatures, even if they preclude a purely crustal origin, indicate that a third component played a role, possibly through AFC processes.

5.2.2. Source contamination

The main mechanism able to modify the composition of the mantle wedge peridotite is metasomatism. Two chief metasomatic agents may be released by the subducted lithosphere: 1) hydrous, solute-rich, likely supercritical fluids generated by subducted slab dehydration, and 2) felsic, SiO_2-rich magmas formed by slab melting. Some elements, such as high field strength elements (HFSE) display a contrasted behaviour with regard to both agents. Indeed, especially when rutile is a residual phase in the subducted slab (>1 and <10) (e.g., Audetat and Keppler, 2005; Brenan et al., 1994, 1995; Tropper and Manning, 2005). Under conditions of <0.7 and typically ≤0.1 (Adam et al., 2014; Green and Adam, 2003), hydrous fluids are unable to transfer significant amounts of Nb from the slab to the mantle wedge, while melts can. Moreover, the felsic melts generated through slab melting at depth show 'adakitic' characteristics with very low Y and Yb contents (Macpherson et al., 2006; Martin, 1999; Martin et al., 2005; Moyen, 2009). As such, the particular metasomatic agent can be explored using a (Nb/Y) vs. (La/Yb) diagram (Fig. 9a, Martin et al., 2010), where Nb tracks fluids and Y and Yb trace melts (leaving residual garnet).

In Fig. 9a the dark grey field includes data from Fiji (Rogers and Setterfield, 1994) and Vanuatu (Monzier et al., 1997), two island arcs

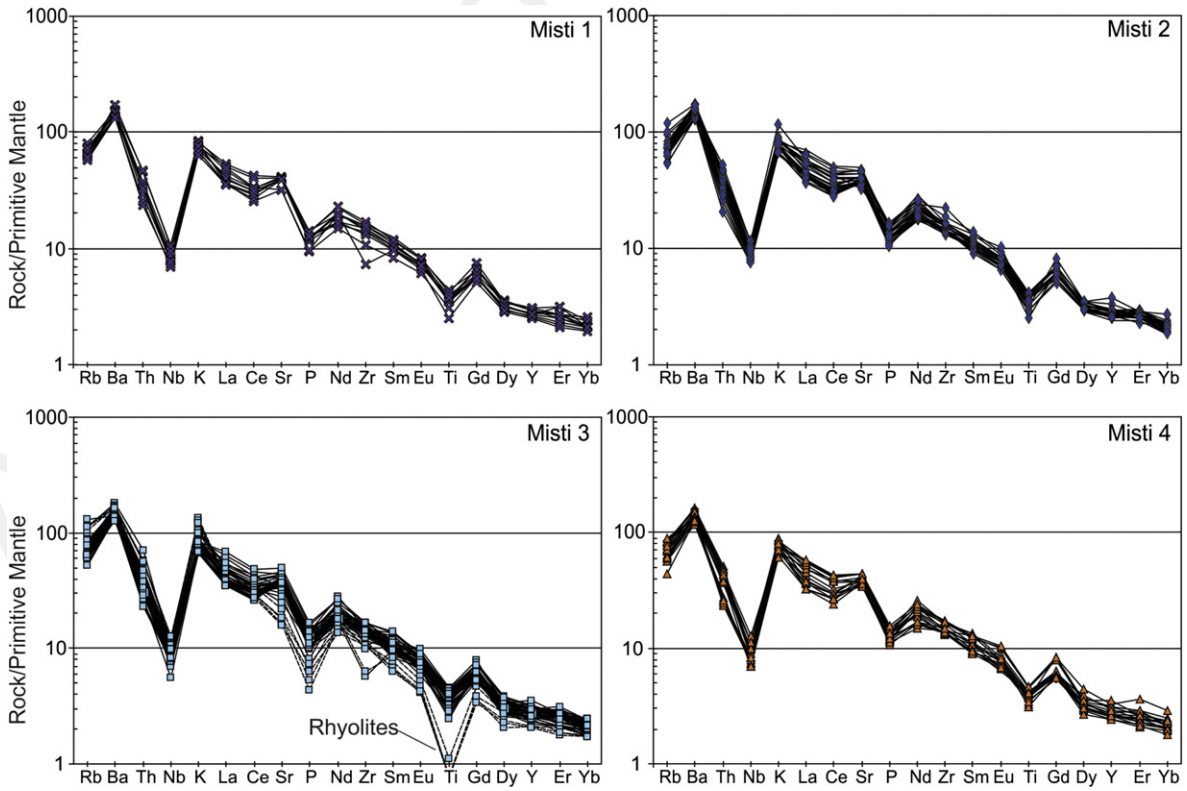

Fig. 6. Multi-element diagrams normalised to primitive mantle (Sun and McDonough, 1989) showing typical trace element patterns of continental arc magmas in El Misti samples.

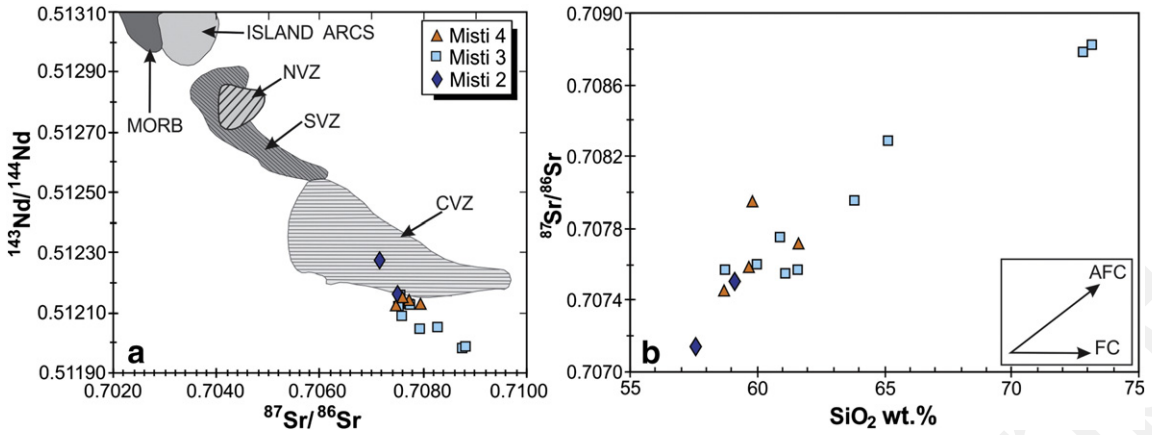

Fig. 7. (a) $^{143}Nd/^{144}Nd$ vs. $^{87}Sr/^{86}Sr$ diagram for El Misti rocks, compared with other published isotopic data for the CVZ, SVZ and NVZ (Davidson et al., 1991). (b) $^{87}Sr/^{86}Sr$ vs. SiO_2 wt.% diagram. Insets schematically depict the evolution of the isotopic composition in the case of a "pure" fractional crystallisation (FC) or a "pure" assimilation–fractional crystallisation (AFC) process.

whose magmatic signatures are free of any continental contamination (Stern, 2010) and the metasomatic agent would solely be fluids produced by sub-solidus dehydration of the subducted slab. In Fig. 9a, the dashed field is that of modern high-Mg andesites and low-silica adakites (Hoffer, 2008; Martin et al., 2005), which result from partial melting of melt-metasomatised mantle peridotite. In this diagram El Misti data do not cluster in a single field. Rather, most data plot in the "felsic melt metasomatism" field and the remainder plot outside near the "fluid metasomatism" field. As such, we infer that metasomatism is mainly due to felsic magma formation. However, as mentioned in previous work (e.g., Davidson et al., 1991; Legendre, 1999; Mamani et al., 2010; Ruprecht and Wörner, 2007) other fluids (i.e. hydrous) may have played a role.

In addition, El Misti lavas show geochemical characteristics (high LREE and Sr, low Y at 9.4–17 ppm, low HREE, with $5.3 < Yb_N < 8.9$, correlated high $(La/Yb)_N$ ranging from 12 to 30 (Table 2, SEM 2) that are similar to those of adakite-type magmas (Defant and Drummond, 1990; Drummond and Defant, 1990; Martin, 1986, 1999; Peacock et al., 1994). Plotting $(La/Yb)_N$ vs.Yb_N (Martin, 1999) suggests adakitic affinities for El Misti samples (Fig. 9b). Moreover, the SiO_2-poorer lavas of El Misti display all the geochemical characteristics of low-silica adakites (LSA), which are considered to be generated by

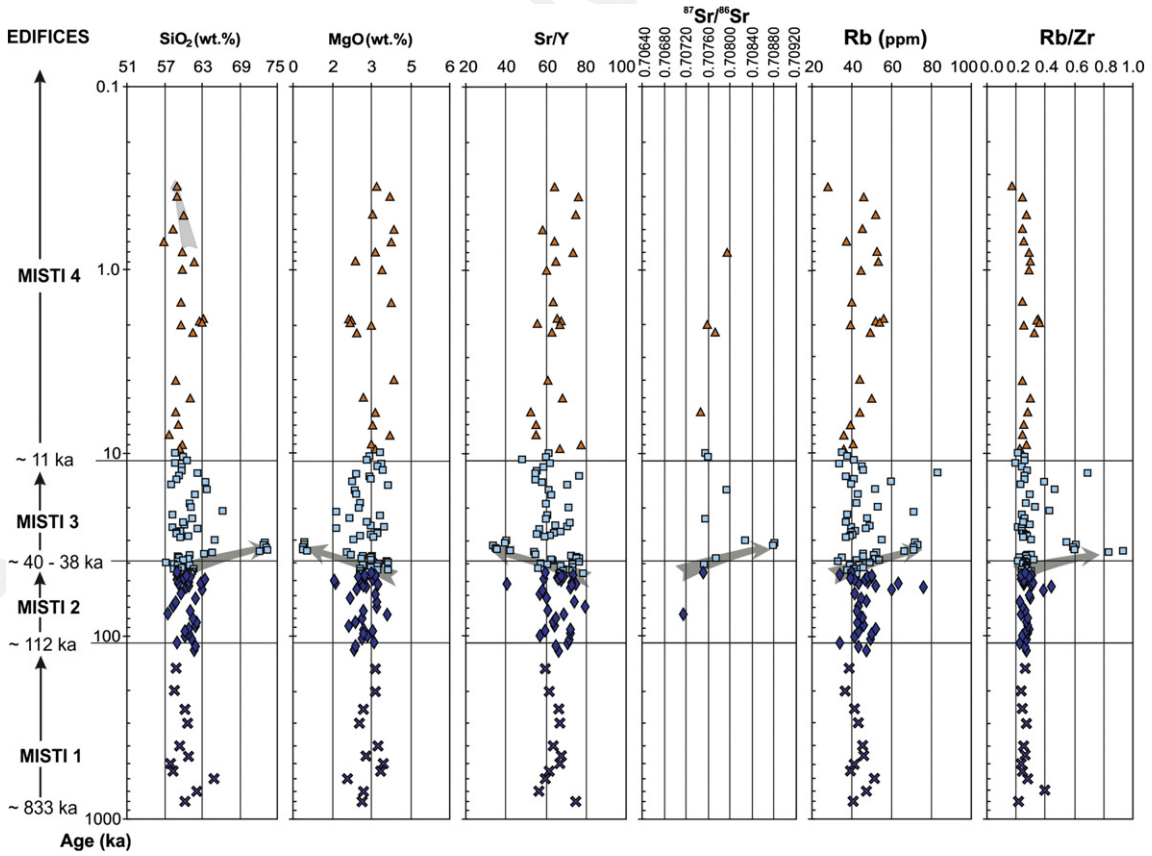

Fig. 8. Compositional changes of El Misti's lavas and juvenile pyroclastic products through time. The chronological axis is inverse-logarithmic to account for higher sampling density and wider compositional range in young eruptive products.

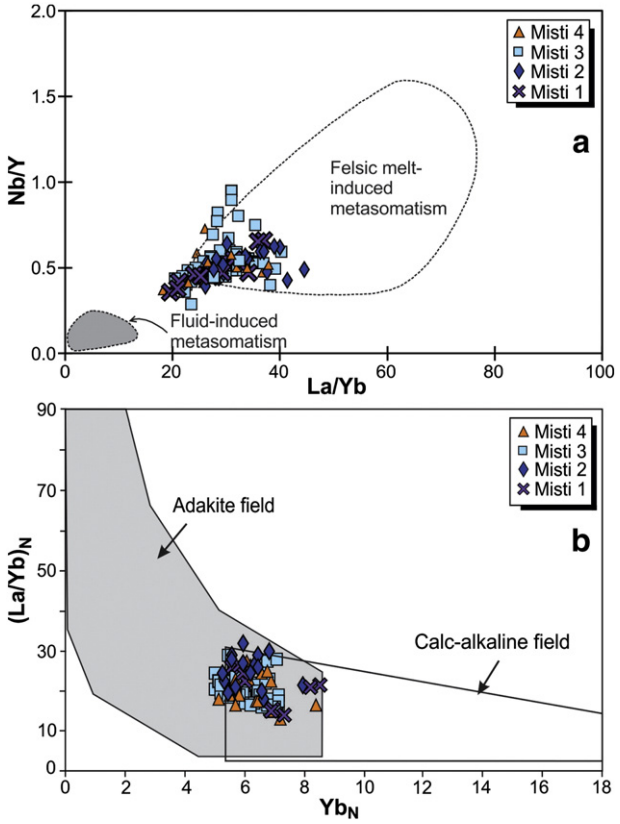

Fig. 9. (a) Plot of Nb/Y vs. La/Yb discriminating magmas generated by melting of a mantle metasomatised by fluids (grey field) or felsic melts (dashed field). Fields after Martin et al. (2010); (b) Plot of $(La/Yb)_N$ vs. Yb_N (Martin, 1999) showing that most data from El Misti lavas overlap the typical calc-alkaline and adakitic fields.

mixing of a mantle source metasomatised by felsic melts (Martin et al., 2005).

On the other hand, the oceanic crust that subducts beneath the northern area of the CVZ is quite old (ca. 40–50 Ma) (Sébrier and Soler, 1991). Under such conditions, the MORB and sediments of the subducted slab are already dehydrated when plunging beneath the volcanic arc, thus impeding their melting (Syracuse et al., 2010). Such conditions led to the alternative proposal that the adakite signature is not inherited from the source, rather it is acquired during magma storage and ascent from the base of the crust (e.g., Castillo, 2006; Delacour et al., 2007; Haschke et al., 2002; Kay et al., 1999; Mamani et al., 2010; Sørensen and Holm, 2008; Thouret et al., 2005).

5.3. Intracrustal events

5.3.1. Fractional crystallisation

Our mineralogical and geochemical data from El Misti highlight the prominent role played by fractional crystallisation processes as expressed by: a) the presence of zoned phenocrysts (plagioclase and clinopyroxene); b) the marked correlation between incompatible elements; and c) the depletion of the magma in compatible elements along differentiation trends. Plotted values are aligned and define sub-vertical trends in log(compatible element) vs. log(incompatible element) diagrams (Fig. 5).

5.3.2. Crustal contamination

In El Misti lavas $^{87}Sr/^{86}Sr$ positively correlates to SiO_2 content (Fig. 7b) and $^{143}Nd/^{144}Nd$ negatively correlates to SiO_2 content. Such relationships are typical of crustal contamination (DePaolo, 1988; Leeman and Hawkesworth, 1986) and are noted not only at El Misti, but are widespread throughout Quaternary CVZ lavas, for which crustal contamination is recognised as a major petrogenetic process (e.g., Davidson et al., 1991; Delacour et al., 2007; Gerbe and Thouret, 2004; Godoy et al., 2014; Hildreth and Moorbath, 1988; Mamani et al., 2010; Sørensen and Holm, 2008; Thorpe et al., 1984). The depth at which this contamination takes place, however, is still debated. Some previous work suggests that contamination occurs in the lowermost crust through MASH-type processes (Davidson et al., 1990; Delacour et al., 2007; Harmon and Hoefs, 1984; Hildreth and Moorbath, 1988), whereas others argue that contamination develops during ascent and storage of the magma through the upper crust (Davidson et al., 1990; Gerbe and Thouret, 2004; James, 1984; Ruprecht and Wörner, 2007).

Kiebala (2008) investigated the lead isotopic system in El Misti lavas ($17.40 < ^{206}Pb/^{204}Pb < 17.84$; $15.52 < ^{207}Pb/^{204}Pb < 15.61$, and $38.37 < ^{208}Pb/^{204}Pb < 38.6$), obtaining values similar to those reported for the regional metamorphic basement (Barreiro and Clark, 1984; Mamani et al., 2010; Wilson, 1989). Previous studies (Aitcheson et al., 1995; Harmon et al., 1984; James, 1982; Mamani et al., 2010; Wörner et al., 1992) also highlighted a clear relationship between the Pb-isotope composition of the metamorphic basement and that of the magmas which ascended through the continental Andean crust. Such Pb isotope data further supports the inference from Sr and Nd isotopic systems that El Misti magmas assimilated significant amounts of the regional metamorphic basement during ascent.

On the other hand, previous studies have proposed that the "adakitic" signature of El Misti lavas might have been acquired during a late stage evolution through mixing and assimilation of a mantle-derived parent magma with a magma generated at high pressure at the base of the continental crust (e.g., Delacour et al., 2007; Haschke et al., 2002; Kay et al., 1999; Mamani et al., 2010; Sørensen and Holm,

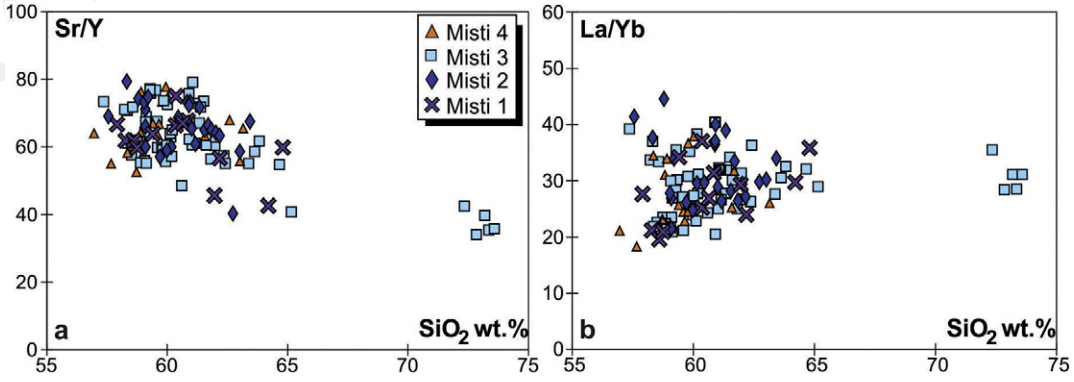

Fig. 10. Plot of (a) Sr/Y vs. SiO_2 wt.% and (b) La/Yb vs. SiO_2 wt.% showing the roles of amphibole and garnet in El Misti magma evolution.

Table 3
Major-element compositions of the parent and daughter magmas for the El Misti series together with results of the mass-balance calculations. The composition of the calculated parent magma is shown for comparison with the hypothetical parent magma. (1 − F) crystallisation rate in %; $\sum r^2$ sum of the residual squares. Major element compositions of rock-forming minerals from El Misti are also given. For each mineral, the average composition (re-calculated on an anhydrous basis) is derived from several analyses. *N* is the number of analyses. Mineral abbreviations: Cpx clinopyroxene, Pl plagioclase, Ol olivine, Amp amphibole, ti-mt titano-magnetite, Ap apatite.

	Parent magma (Co) MIS-0204	Daughter magma (Cl) MI-0508	Calculated parent magma	Cpx	Pl	Ol	ti-mt	Ap	Amp
N				12	16	8	10	6	15
SiO_2 (wt.%)	58.86	73.37	59.26	52.03	52.66	38.89	0.09	0.18	42.72
TiO_2	0.91	0.17	1.10	0.66	0.04	0.02	11.25	0.06	2.84
Al_2O_3	17.34	15.12	17.50	2.16	28.74	0.01	2.83	0.03	12.18
Fe_2O_3	6.75	1.52	6.08						
FeO				8.44	0.8	20.98	75.40	1.21	10.36
MnO	0.10	0.09	0.10	0.24	0.17	0.27	0.40	0.05	0.08
MgO	3.40	0.40	3.40	15.49	0.07	40.09	3.57	0.12	15.17
CaO	6.07	1.34	6.08	20.40	12.30	0.11	0.07	54.32	11.48
Na_2O	4.15	4.17	4.03	0.34	4.48	0.01	0.05	0.17	2.39
K_2O	2.12	3.68	2.05	0.02	0.29	0.01	0.01	0.01	0.67
P_2O_5	0.30	0.14	0.32					42.72	0.02
% cumulate					52.53		6.64	1.02	39.81
(1 − *F*) %			53.09						
$\sum r^2$			0.041						

2008; Thouret et al., 2005). The relatively low Yb and Y contents of El Misti lavas suggest the influence of garnet (± amphibole) crystallisation, a proxy for crustal thickening (Mamani et al., 2010). If slab melting is excluded, the "adakitic" characteristics can only be provided by crustal contamination, for instance through melting at depth within the garnet stability field. Such a scenario, however, conflicts with the dataset presented here. In particular, the Yb content does not correlate to SiO_2 content (Fig. 4) as would be expected for contamination by the continental crust. Similarly, both La/Yb and Sr/Y ratios, whose high values are principal adakite fingerprints (Defant and Drummond, 1990; Martin et al., 2005), are not positively correlated to SiO_2 (Fig. 10). Assuming the adakitic characteristics are exclusively generated by crustal contamination mechanisms, these ratios should be positively correlated to SiO_2, which is clearly not the case at El Misti. In addition, our results reveal that the Sr/Y ratios at El Misti are anticorrelated to SiO_2. This observation is supported by the fact that the adakitic characteristics are also present in less differentiated magmas (e.g., JMI-159).

5.4. Modelling of magmatic processes

In order to explore and check their reliability, different petrogenetic mechanisms have been tentatively quantified using the methodology of Janoušek et al. (2015). The model aims at testing the relationship between the more evolved magma and the less differentiated magma.

5.4.1. Simple fractional crystallisation

The Misti 3 samples were selected for modelling because they show the widest range of differentiation (57% < SiO_2 < 74 wt.%). As proposed by Janoušek et al. (2015), our modelling has included two steps: first, the mass-balance algorithm of Störmer and Nicholls (1978) to compute modal and geochemical compositions of the cumulative assemblage based on major elements (Table 3). Second, the calculated values are entered into trace-element modelling equations of Rayleigh (1896) (details on mathematical procedures are given in Janoušek et al., 2015). Samples Mis-0204 (58.9 wt.% SiO_2) and Mi-0508 (73.4 wt.% SiO_2) represent the least and most differentiated Misti-3 magmas, respectively (Table 4). Composition of the potential cumulative minerals are those of the phenocrysts. However, as plagioclase is generally zoned, we used two 'pure' end-members (Ab and An) that were subsequently recombined. The same approach holds for the Fe–Ti oxides which are considered as a 'solid solution' of magnetite and rutile, irrespective of the actual mineral present (titano-magnetite) (Janoušek et al., 2015). Data from major element compositions for the fractioning minerals and modelling results are provided in Table 3. The strength of the adjustment between the theoretical model and the data is expressed for major elements as: $\Sigma r^2 = \Sigma\ (m_i\_c_i)^2$, where m_i is the measured

Table 4
Trace element compositional data of El Misti series parent and daughter magmas used for fractional crystallisation modelling with Rayleigh (1896) equations. The composition of the calculated daughter magma is given for comparison with the hypothetical daughter magma. Partition coefficients (K_D) for andesites used for trace element modelling are given. K_D for amphibole is from Sisson (1994) and Martin (1987). K_D for clinopyroxene, plagioclase, Fe-Ti oxide and apatite are from Mahood and Hildreth (1983), Nash and Crecraft (1985), Martin (1987), Bacon and Druitt (1988), Sisson (1991), and Ewart and Griffin (1994).

Elements	Parent magma (Co) MIS-0204	Daughter magma (Cl) MI-0508	Calculated daughter magma	Cpx	Pl	Ol	ti-mt	Ap	Amp
La	26.8	24.5	25.7	0.31	0.4	0.01	0.22	28	0.4
Ce	51.5	48.6	46.1	0.5	0.27	0.02	0.26	35	0.5
Nd	22.2	18.2	18.5	1.4	0.19	0.0003	0.3	61	1.1
Sm	4.2	2.8	3.0	1.67	0.13	0.0048	0.35	64	1.1
Eu	1.4	0.7	0.9	1.56	1.9	0.01	0.26	30	2
Gd	3.8	2.0	2.5	1.85	0.13	0.0029	0.28	64	1.8
Dy	2.3	1.7	1.7	1.93	0.064	0.002	0.28	58	2
Er	1.2	0.8	1.0	1.3	0.055	0.062	0.22	40	1.9
Yb	1.2	0.9	1.0	3	0.11	0.03	0.24	22	1.9
Rb	34	71	58	0.03	0.04	0.062	0.18	0.0001	0.026
Ba	962	1151	1260	0.13	1.05	0.02	1E−05	2	0.8
K	17,613	30,536	29,324	0.008	0.13	0.0056	0.96	1E−05	0.333
Nb	5	8	8	0.3	1.3	0.11	1E−05	1E−05	0.25
Sr	868	333	382	0.1	2303	0.07	1E−05	1E−05	0.414
Zr	170	119	193	0.33	0.15	0.02	1E−05	0.64	0.4
Ti	5448.6	1011.0	1925	0.78	0.019	0.019	1.5	1E−05	4.2
Y	14	9.4	10.2	1	0.51	0.018	0.0001	1E−05	4

Table 5
Compositional data of El Misti series parent and daughter magmas used to model AFC processes, along with calculated daughter magma composition. Charcani gneiss data are from Boily et al. (1989) and (2) Boily et al. (1990).

Elements	Parent magma (Co) MIS-0204	Daughter magma (Cl) MI-0508	Calculated daughter magma (AFC modelling)	Result AFC modelling normalised to primitive mantle	Contaminant (Charcani gneiss) This study	(1) and (2) (Charcani gneiss)
La	26.8	24.5	24.5	35.7		63
Ce	51.5	48.6	49.1	27.6	65.1	n.d.
Nd	22.2	18.2	18.6	13.8	41	46
Sm	4.2	2.8	2.7	6.2	9.2	8.8
Eu	1.4	0.7	0.7	4.2	1.7	n.d.
Gd	3.8	2.0	2.1	3.5	9	n.d.
Dy	2.3	1.7	1.5	2.1	9.7	n.d.
Er	1.2	0.8	0.8	1.7	5.7	n.d.
Yb	1.2	0.9	0.8	1.7	5	3
Rb	34	71	67	105.9		120
Ba	962	1151	1121	160.4		1700
Nb	5	8	7	9.7	17.8	n.d.
Sr	868	333	330	15.6	319	250
Zr	170	119	120	10.7		239
Y	14	9.4	9.4	2.1	56.8	n.d.
Th	2.5	3.8	3.3	39.2		15

concentration and c_i is the calculated concentration of oxide *i*. Generally, values of $\Sigma r^2 > 10$ suggest that the model is not acceptable, while values <1 are considered satisfactory results. Lower values of Σr^2 further suggest a better correlation between the model and data (Janoušek et al., 2015) (Table 5).

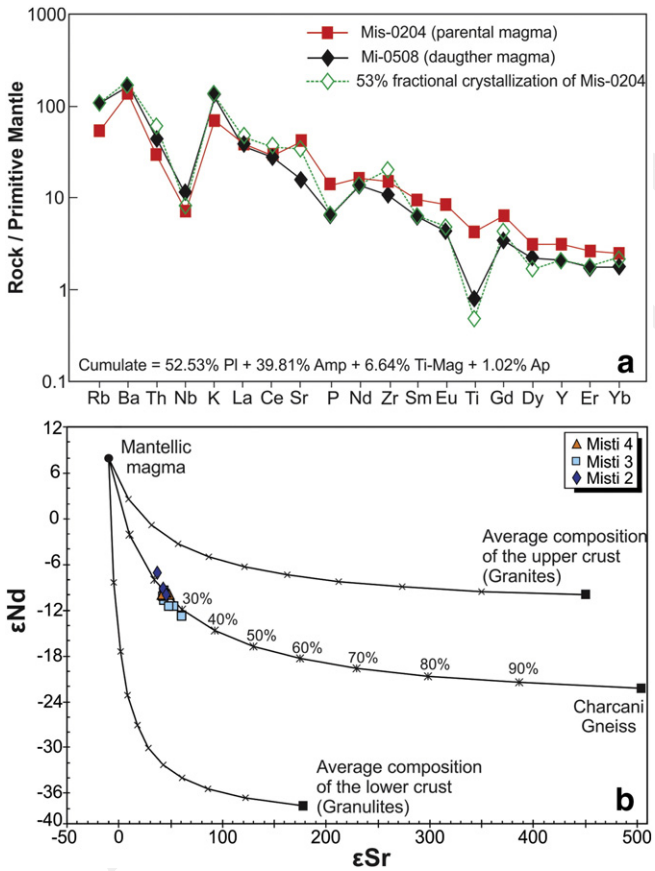

Fig. 11. (a) Theoretical trace element pattern obtained by 53.0% of fractional crystallisation from a magma having the composition of sample Mis0204 (i.e. 58.9 wt.% SiO_2) to obtain the most evolved lava of El Misti series (Mi0508: 73.4 wt.% SiO_2). Values for normalisation to the primitive mantle are from Sun and McDonough (1989). (b) Plot of ε_{Nd} vs. ε_{Sr} between a mafic pole, whose composition is that of a mafic magma generated by partial melting of a mantle wedge (after Boily et al., 1990), and three potential contaminants including average upper and lower crust (after Faure, 1977) and the Precambrian Charcani gneiss (Boily et al., 1989, 1990; James, 1982) of the Western Cordillera basement. Each small bar on the mixing curves corresponds to 10% increments of magma mixing.

Modelling of major elements behaviour yields an excellent fit ($\Sigma r^2 = 0.041$), with the cumulate consisting of 52.53% Pl (An48) + 39.81% Amp + 6.64% Ti-Mag + 1.02% Ap, and the degree of crystallisation (1 − F) being 53.09%. Notably, olivine and pyroxene, while present in some lavas, do not play a significant role (if any) in the fractional crystallisation process.

Our modelling of the trace elements fits the analytical data relatively well except for Sr and Zr (Fig. 11a and Table 4), both of which the model predicts to be poorly compatible to incompatible. In contrast, the opposite is observed in the Sr and Zr concentrations of Misti 3 samples. Zircon fractionation, which is not accounted for in the model, may explain the difference between the observed Zr concentrations and those predicted by the model. We calculate that only 0.022% zircon

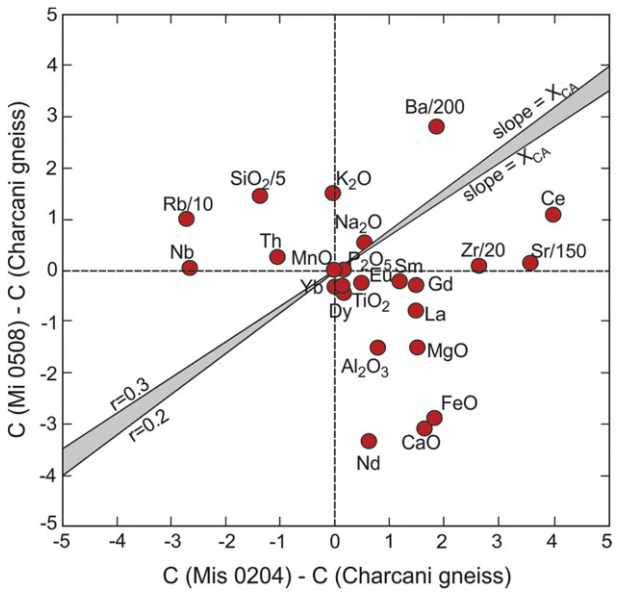

Fig. 12. Results of a model testing the hypothesis that a differentiated magma M (Mi-0508) can be produced by mixing or contamination of a poorly differentiated magma B (Mis-0204) with the "Charcani gneiss" A. This test is based on the simple mixing equation: $C_M = X_A.C_A + (1 - X_A).C_B$, where X_A is the degree of contamination; C_A, C_B, and C_M the concentration of one element in A, B, and M, respectively. From this equation the degree of contamination is $X_A = (C_M - C_B)/(C_A - C_B)$. In the graphical representation X_A is given by the slope of the mixing line. In the case of perfect mixing all data should occur on a single straight line (Fourcade and Allègre, 1981), which is not the case in this plot. Consequently, contamination of El Misti parental magmas by the Charcani gneiss cannot be the main process that controls the evolution of the magmatic suite.

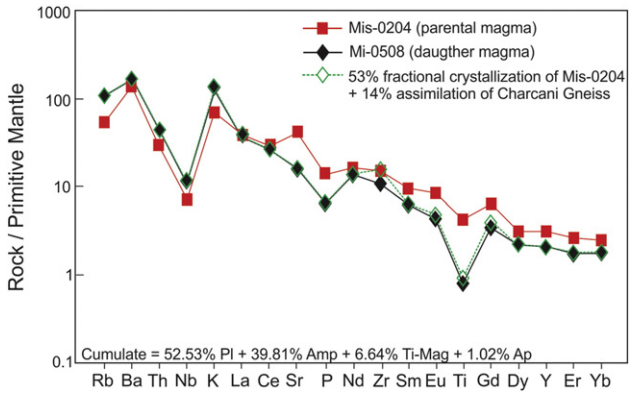

Fig. 13. Theoretical mantle normalised trace element-diagram obtained through modelling assimilation–fractional crystallisation (AFC) for a ρ value (ratio of assimilated material to crystallised material) of 0.2 to 0.3 and the "Charcani gneiss" as the contaminant. Co is the concentration in the parental magma, Cl is the concentration in the resulting magma, and (1 − F) is the degree of crystallisation obtained from fractional crystallisation modelling. The modal composition of the cumulate is also shown. Values for normalisation to the primitive mantle are from Sun and McDonough (1989).

fractionation is sufficient to adjust the calculated Zr content to that of sample Mi-0508. The difference between the observed and modelled Sr concentrations remains ambiguous, except that a Sr-rich component possibly plays a role in the process. Consequently, based on major and trace elements, we may interpret most of the magmatic evolution of El Misti magmas in terms of simple fractional crystallisation of plagioclase + amphibole with subordinate amounts of titanomagnetite + apatite. Our isotope data from the same samples, however, support an opposite interpretation, as discussed below.

5.4.2. Continental crust assimilation

As mentioned above, the ca. 2 ka BP pumice from the Misti 4 stage is texturally banded and contains feldspar with inverse zoning and sieve textures that suggest compositional instability and magma heterogeneity during crystal growth processes. Such heterogeneity can occur as a result of alteration of the magma composition or changes in pressure–temperature conditions. Previous interpretations (e.g., Coombs et al., 2000; Kawamoto, 1992) of such resorption textures suggest that they result from mechanical magma mixing or mingling processes, which may imply thermal effects (Ruprecht and Wörner, 2007). Similar interpretations are applied to Peruvian Plio-Quaternary lavas for which most geochemical work identifies crustal assimilation as a major process governing the magmatic evolution from andesites to rhyolites (Barreiro and Clark, 1984; Delacour et al., 2007; James, 1982; Thorpe et al., 1984; Thouret et al., 2005; Vatin-Pérignon et al., 1992). In such cases, the systematic and significant contamination is correlated with the overthickened CVZ crust (65–70 km, Barazangi and Isacks, 1976; Kono et al., 1989), but the actual structural level where these processes take place is still controversial (e.g. Davidson et al., 1991; Delacour et al., 2007; Sørensen and Holm, 2008).

The $^{87}Sr/^{86}Sr$ and $^{143}Nd/^{144}Nd$ ratios are negatively correlated (Fig. 7), while the positive correlation of $^{87}Sr/^{86}Sr$ to SiO_2 suggests typical crustal contamination processes. El Misti volcano and the Arequipa Massif rest upon a Proterozoic granulitic basement known locally as the "Charcani gneiss" (Guevara, 1969; Ramos, 2008). The basement is exposed on the west flank of the Western Cordillera and is present below the northern Bolivian altiplano (Loewy et al., 2004; Tosdal, 1996), and arguably occurs at depth beneath the calc-alkaline volcanic arc of southern Peru (Harmon et al., 1981). The composition and origin of the Charcani gneiss are characterised and it is considered the best candidate for contamination of CVZ arc magma (Boily et al., 1989, 1990; James, 1982; Loewy et al., 2004; Mamani et al., 2008; Tosdal, 1996; Wasteneys et al., 1995; Wilson, 1989). We test such a hypothesis for El Misti lavas assuming a simple two-component mixing. One component is a mafic magma generated by partial melting of a mantle wedge that is slightly enriched in LILE (see details in Boily et al., 1990), while the other component is the continental crust. We test three potential continental crust contaminants consisting of average upper and lower crusts (Faure, 1977) and the Charcani gneiss from the Western Cordillera basement (Boily et al., 1989, 1990; James, 1982). The latter likely occurs at a mid to upper crustal level near and below El Misti volcano (De la Cruz and Herrera, 2000; Guevara, 1969). The results (Fig. 11b) suggest that the average upper and lower crusts are not realistic crustal contaminants. In contrast, contamination by the Charcani gneiss can reproduce the isotopic characteristics of El Misti lavas. The calculated degree of crustal contamination ranges from 20 to 30%, but only silica-rich lavas from Misti 3 suggest contamination over 25%.

However, when tested with both major and trace elements this quantitative isotope-based model fails to convincingly predict elemental behaviour. Fig. 12 shows mixing (Fourcade and Allègre, 1981), in which simple binary mixing should result in a linear trend passing through the origin. The grey field represents theoretical compositions for 20 to 30% contamination by the Charcani gneiss. Noticeably, the analytical data conflicts with the modelling results, implying that simple contamination of the El Misti parent magma by the Charcani gneiss is not the only process that controls the magma's evolution. Consequently, to account for isotopic as well as major and trace element constraints, we test alternative models that combine assimilation–fractional crystallisation (AFC) scenarios.

5.4.3. Assimilation–fractional crystallisation (AFC)

Fractional crystallisation processes are generally combined with the assimilation of the wall rocks surrounding the magma chamber (DePaolo, 1981). The amount of assimilated material correlates to the quantity of magma that has crystallised through cooling. AFC modelling (DePaolo, 1981) requires applying parameters for simple fractional crystallisation models such as a parent magma (sample Mis-0204), daughter magma (sample Mi-0508), modal composition of the cumulate = 52.5% Pl (An_{48}) + 39.8% Amp + 6.6% Ti-Mag + 1.0% Ap, and degree of fractional crystallisation ((1 − F) = 53%). As deduced by the isotope data, the Charcani gneiss is selected as the contaminant and the proportion of the rate of assimilation/rate of crystallisation (ρ) is set in the range of 0.2 to 0.3.

A multi-element plot (Fig. 13) comparing our analytical data to the results of AFC modelling reveals an excellent fit for ρ ≤ 0.22, which corresponds to an assimilation of ≤14 vol.% (proportion of crust added to the original magma and calculated following Aitcheson and Forrest, 1994). The AFC modelling yields a better fit to the data, in particular with Sr, than simple fractional crystallisation, but the difference between both approaches is small and within uncertainty for most elements. As such, if simple fractional crystallisation fails to account for the isotope behaviour, the latter is reliably predicted by an AFC mechanism. Nonetheless, the model predicts 20 to 30% contamination based solely on isotope data while major and trace elements suggest less than 22% contamination. Such a contradiction arises because the degree of contamination is calculated using a mantle-like source for isotopes and a differentiated magma (Mis-0204) for major and trace elements.

We emphasise that the Charcani gneiss and the least differentiated El Misti lava (MIS-0204) have similar Yb and La contents (1.2 and 26 ppm, respectively) and consequently contamination by the Charcani gneiss is unlikely to yield the adakitic characteristics of the lavas. Accordingly, such adakitic characteristics are not acquired late in the magma's evolution (i.e., by upper crustal contamination), rather they are congruent with a mantle source. The subducting oceanic crust, however, is ca. 40–50 Ma (Sébrier and Soler, 1991), suggesting that the slab is likely too cold for melting (Peacock et al., 1994). This results in conflicting scenarios. Notwithstanding, mantle metasomatism is not

necessarily contemporaneous with the melting event and may have taken place tens of milllions of year before, when the subduction was hotter (younger subducted crust), as proposed by Rapp et al. (1999, 2010) and Martin et al. (2005, 2010).

5.5. Temperature and pressure conditions of the crustal processes

The physical conditions that prevailed during magma crystallisation are tentatively established through temperature and pressure estimates.

5.5.1. Temperature

We estimate equilibrium temperatures for orthopyroxene and clinopyroxene using Putirka's (2008) method, which is appropriate for calc-alkaline magmas of andesitic to rhyolitic compositions within a temperature range of 700 to 1700 ± 30 °C. Putirka (2008) examined a set of 311 experimental pyroxene pairs and obtained a Fe-Mg exchange coefficient between clinopyroxene and orthopyroxene defined as:

$$K_D(Fe-Mg)^{cpx-opx} = \left(X_{Fe}^{cpx}/X_{Mg}^{cpx}\right)/\left(X_{Fe}^{opx}/X_{Mg}^{opx}\right)$$

where X_i^j refers to the mole fraction of component i in phase j. Discarding outlier data outside of 3σ yielded a $K_D(Fe\text{-}Mg)^{cpx\text{-}opx}$ of 1.09 ± 0.14, which is proposed to evaluate the equilibrium conditions for two pyroxenes. This method, however, is only applicable when the two pyroxenes coexist in equilibrium conditions. Pyroxenes pairs in some El Misti samples, however, did not yield equilibrium values ($K_D(Fe\text{-}Mg)^{(cpx\text{-}opx)} = 1.09 \pm 0.14$) and as a result such non-equilibrium pairs were excluded.

Cores of pyroxenes from El Misti andesites yield a crystallisation temperature of 965 ± 45 °C (n = 36). The lower temperature limit further grossly correlates negatively to SiO_2 contents in the lavas.

In addition, crystallisation temperature is estimated using the amphibole-based geothermometer of Ridolfi et al. (2010), which is based on a rigorous analysis of the physical–chemical, compositional and textural relationships of amphibole stability. The geothermometer applies to amphibole-bearing calk-alkaline magmas under a range of crystallisation temperatures from 550 to 1120 °C and for pressures <1200 MPa. By adding fractions of the amphibole's major cations to Si, Ridolfi et al. (2010) derived a silicon index (Si*) which, combined with temperature (T) estimates (T (°C) = −151.487Si* + 2041), yields a higher linear regression coefficient (i.e. $R^2 = 0.84$).

Ridolfi et al.'s (2010) index is defined as: $Si^* = Si + (^{[4]}Al/15) - (2^{[4]}Ti) - (^{[6]}Al/2) - (^{[6]}Ti/1.8) + (Fe^{3+}/9) + (Fe^{2+}/3.3) + (Mg/26) + (^{B}Ca/5) + (^{B}Na/1.3) - (^{A}Na/15) + (^{A}[Na + K]/2.3)$.

The mineralogy of El Misti's lavas suggests that amphibole crystallised predominantly at equilibrium with the surrounding melt. We estimate crystallisation temperatures of the high-Al amphiboles using Ridolfi et al.'s (2010) geothermometer, which provides reliable temperature values (Kiss et al., 2014). To estimate such temperatures we applied the Amp-TB.xls spreadsheet of Ridolfi et al. (2010) and obtained temperatures of 951 ± 33 °C (n = 85) for El Misti andesites and slightly lower values of 941 ± 25 °C (n = 14) for the dacites. Notably, temperature estimates derived from Ridolfi et al.'s (2010) method match the temperature range inferred from the two-pyroxene geothermometer.

5.5.2. Pressure

Many available geobarometers are based on the total aluminium (Al^T) content in amphibole, which is known to positively correlate to pressure (Hammarstrom and Zen, 1986; Hollister et al., 1987; Schmidt, 1992). Recently, Ridolfi et al. (2010) proposed a geobarometer that applies the same principles and is adapted to calc-alkaline compositions in which calcic-amphiboles have Al# ≤ 0.21 and Mg# > 0.5 ($Al\# = Al^{VI}/Al^T$; $Mg\# = (Mg/(Mg + Fe^{2+}))$. The confining pressure (P) has been calculated with the following equation:

$$\text{Pressure } P(MPa) = 19.209e^{(1.438Altot)}, R^2 = 0.99$$

The single amphibole geobarometer of Ridolfi et al. (2010) is commonly used to constrain magma chambers' depths beneath intermediate arc volcanoes (e.g., Chambefort et al., 2013; Costa et al., 2013; Scott et al., 2012; Walker et al., 2013). In this case, amphiboles with wide compositional range could imply either a vertically extended magma reservoir or separated magma chambers at different depths. Results of these geobarometers were recently tested using compositionally zoned amphiboles and experimental data which revealed that the large calculated pressure variations provided by the Ridolfi et al. (2010) geobarometer is only apparent and reflect crystallisation of amphiboles at different temperatures and/or from different magmas (Erdmann et al., 2014; Kiss et al., 2014; Shane and Smith, 2013). The pressure estimates obtained for bimodal amphibole populations in arc magmas can be explained by crystallisation in cold, felsic magmas and hot, mafic magmas, respectively rather than by formation in two reservoirs at different depths (Erdmann et al., 2014; Kiss et al., 2014). Thus, careful textural and compositional investigation, involving a comparison of the amphibole's textures and compositions with experimental data is recommended before conducting such thermobarometric calculations.

Our mineralogical study showed that amphibole crystallisation occurred primarily at equilibrium with the surrounding melt and resulted in a normal zoning. To determine amphibole crystallisation pressures we used the Amp-TB.xls spreadsheet of Ridolfi et al. (2010). Results indicate that El Misti amphibole crystallised at pressures ranging from 237 ± 26 to 413 ± 45 MPa which, assuming a crustal density in the range of 2700 to 2900 kg/m^3 (Kono et al., 1989), suggest crystallisation depths of about 9 ± 1 km to 15 ± 2 km. These estimates concur with those of Tepley et al. (2013), whose geobarometric analysis also infers the presence of a small-volume rhyolitic reservoir located at a crustal depth of ~3 km (<100 MPa) and an andesitic reservoir at a depth of ~7–12 km (~200–350 MPa).

In addition, early crystallisation of Fe-Ti oxides, the ubiquitous occurrence of amphiboles (3–15 vol.%) and crystallisation of clinopyroxene prior to plagioclase are all evidence for high P_{H2O}. Similarly, the relatively high AlIV/AlVI ratio in clinopyroxenes (0.8–18.3) in conjunction with their low Na_2O (0.7–0.01 wt.%) and TiO_2 (0.15–0.54 wt.%) contents further support a crystallisation scenario at low pressure in a relatively shallow magma chamber (Aoki and Shiba, 1973; Wass, 1979).

6. Conclusions

El Misti volcano has displayed diverse eruptive styles over the past 112–833 ka: relatively high frequency of explosive eruptions, widespread tephra falls, emplacement of infrequent voluminous ignimbrites, caldera collapse, and lava emplacement. Throughout such a diverse eruptive history the composition of El Misti's erupted lavas remained fairly homogeneous (andesite-dacite) with the only exception being the volcano's most differentiated rhyolitic products emplaced between 34 and 31 ka (Misti 3). From our mineralogical and geochemical data and subsequent modelling, we summarise the petrogenetic history of El Misti as follows:

- Fairly mafic magmas generated by partial melting of the mantle wedge rise and accumulate in shallow-depth crustal reservoirs (9–15 km) where they mainly experience AFC differentiation and eventually magma mixing or mingling as also suggested by Tepley et al. (2013).
- The mantle wedge source of the parental magmas was previously enriched (metasomatised) by a felsic melt of adakitic composition rather than hydrous fluids.

- Trace element and isotope signatures suggest that the Charcani gneiss from the Proterozoic basement is the most likely crustal contaminant (Delacour et al., 2007; Gerbe and Thouret, 2004; Mamani et al., 2010; Sørensen and Holm, 2008; Thorpe et al., 1984; Wilson, 1989). We estimate the degree of such crustal contamination generally remained below 20%, only peaking at ~30% during the Misti 3 stage (34–31 ka).

The petrogenetic diversity revealed in this study mirrors the wide variety of past eruptive behaviour inferred from previous geological work, and suggests such irregularity in both eruption style and magnitude will continue in the future. While moderate-sized eruptions are more likely to occur for the next event, sub-Plinian to Plinian eruptions are also possible, even with andesitic magma compositions (58–59 wt.% SiO_2) as illustrated by the ca. 2 ka BP event.

The high magma output rate estimated in previous work implies that any future eruption may produce significant volumes of lavas and/or tephras, a situation which would inevitably impact the nearby city of Arequipa (~1,000,000 inhabitants), whose northwestern and northeastern suburbs are located a mere 9 km from the crater.

Supplementary data to this article can be found online at http://dx.doi.org/10.1016/j.lithos.2016.11.009.

Acknowledgements

This work is part of the first author's PhD and was funded by the French Institut de Recherche pour le Développement (IRD), Département Soutien et Formation des Communautés Scientifiques du Sud (DSF) hosted at Laboratoire Magmas et Volcans (LMV) and the Instituto Geológico Minero y Metalúrgico of Peru (INGEMMET). It has been completed within IRD's joint research programs 'Jeune Équipe associée à l'IRD' and the Laboratoire Mixte International (LMI) 'Séismes et Volcans dans les Andes'. We thank P. Soler, G. Hérail, and L. Fidel for administrative and logistical support in France and Peru, J.P. Eissen and J.L. Devidal for sampling and technical help with microprobe analyses and our colleagues at the Observatorio Vulcanológico at INGEMMET in Arequipa for continuous support during field campaigns. C. Harpel offered a final revision of the text to improve the language. Thoughtful reviews by Guillaume Jacques and Aurélie Germa improved the manuscript, and editorial handling by Andrew Kerr was much appreciated.

References

Adam, J., Locmelis, M., Alfonso, H.C., Rushmer, T., Fiorentini, M.L., 2014. The capacity of hydrous fluids to transport and fractionate incompatible elements and metals within the Earth's mantle. Geochemistry, Geophysics, Geosystems 15 (6), 2241–2253.

Aitcheson, S.J., Forrest, A.H., 1994. Quantification of crustal contamination in open magmatic systems. Journal of Petrology 35, 461–488.

Aitcheson, S.J., Harmon, R.S., Moorbath, S., Schneider, A., Soler, P., Soria Escalante, E., Steele, G., Swainbank, I., Wörner, G., 1995. Pb isotopes define basement domains of the Altiplano, central Andes. Geology 23, 555–558.

Aoki, K., Shiba, I., 1973. Pyroxenes from lherzolite inclusions of Itinomegata, Japan. Lithos 6, 41–51.

Audetat, A., Keppler, H., 2005. Solubility of rutile in subduction zone fluids, as determined by experiments in the hydrothermal diamond anvil cell. Earth and Planetary Science Letters 232 (3–4), 393–402.

Bacon, C.R., Druitt, T.H., 1988. Compositional evolution of the zoned calc-alkaline magma chamber of Mount Mazama, Crater Lake, Oregon. Contributions to Mineralogy and Petrology 98, 224–256.

Barazangi, M., Isacks, B., 1976. Subduction of the Nazca plate beneath Peru: evidence from spatial distribution of earthquakes. Geophysical Journal of the Royal Astronomical Society 57, 537–555.

Barreiro, B.A., Clark, A.H., 1984. Lead isotopic evidence for evolutionary changes in magma-crust interaction, Central Andes, southern Peru. Earth and Planetary Science Letters 69, 30–42.

Boily, M., Brooks, C., Ludden, J.N., James, D.E., 1989. Chemical and isotopic evolution of the coastal batholith of southern Peru. Journal of Geophysical Research B 94 (9), 12483–12498.

Boily, M., Ludden, J.N., Brooks, C., 1990. Geochemical constraints on the magmatic evolution of the pre- and post-Oligocene volcanic suites of southern Peru: implication for the tectonic evolution of the central volcanic zone. Geological Society of America Bulletin 102 (11), 1565–1579.

Brenan, J.M., Shaw, I.H.F., Phinney, D.L., Ryerson, F.J., 1994. Rutile-fluid partitioning of Nb, Ta, Zr, U and Th: implications for high-field-strength element depletions in island-arc basalts. Earth and Planetary Science Letters 128, 327–339.

Brenan, J.M., Shaw, I.H.F., Ryerson, F.J., Phinney, D.L., 1995. Mineral-aqueous fluid partitioning of trace elements at 900 °C and 2.0 GPa: constraints on the trace element chemistry of mantle and deep crustal fluids. Geochimica et Cosmochimica Acta 59 (16), 3331–3350.

Castillo, P.R., 2006. An overview of adakite petrogenesis. Chinese Science Bulletin 51 (3): 257–268. http://dx.doi.org/10.1007/s11434-006-0257-7.

Chambefort, I., Dilles, J.H., Longo, A.A., 2013. Amphibole geochemistry of the Yanacocha volcanics, Peru: evidence for diverse sources of magmatic volatiles related to gold ores. Journal of Petrology 54 (5), 1017–1046.

Chavéz Chavéz, J.A., 1992. La erupción del volcán Misti, pasado, presente, futuro: Arequipa. Impresiones Zenit, Arequipa-Peru (158 pp.).

Cobeñas, G., Thouret, J.C., Bonadonna, C., Boivin, P., 2014. Reply to comment on: Cobeñas, G., Thouret, J.-C., Bonadonna, C., Boivin, P., 2012. The c. 2030 yr BP plinian eruption of El Misti volcano, Peru: eruption dynamics and hazard implications. Journal of Volcanology and Geothermal Research 275C:103–113. http://dx.doi.org/10.1016/j.jvolgeores.2014.02.014.

Cocherie, A., 1986. Systematic use of trace element distribution on patterns in log–log diagrams for plutonic suites. Geochimica et Cosmochimica Acta 50, 2517–2522.

Coombs, M.L., Eichelberger, J.C., Rutherford, M.J., 2000. Magma storage and mixing conditions for the 1953-1974 eruptions of Southwest Trident volcano, Katmai National Park, Alaska. Contributions to Mineralogy and Petrology 140, 99–118.

Costa, F., Andreastuti, S., Bouvet de Maisonneuve, C., Pallister, J.S., 2013. Petrological insights into the storage conditions, and magmatic processes that yielded the centennial 2010 Merapi explosive eruption. Journal of Volcanology and Geothermal Research 261, 209–235.

Cotten, J., Le Dez, A., Bau, M., Carroff, M., Maury, R.C., Dulski, P., Fourcade, S., Bohn, M., Brousse, R., 1995. Origin of anomalous rare-earth element and yttrium enrichments in subaerial exposed basalts: evidence from French Polynesia. Chemical Geology 119, 115–138.

Davidson, J.P., de Silva, S.L., 1995. Late Cenozoic magmatism of the Bolivian Altiplano. Contributions to Mineralogy and Petrology 119, 387–408.

Davidson, J.P., McMillan, N.J., Moorbath, S., Wörner, G., Harmon, R.S., López Escobar, L., 1990. The Nevados de Payachata volcanic region (18°S/69°W, N. Chile) II. Evidence for widespread crustal involvement in Andean magmatism. Contributions to Mineralogy and Petrology 105, 412–432.

Davidson, J.P., Harmon, R.S., Wörner, G., 1991. The source of the Central Andes magmas; some considerations. Andean Magmatism and Its Tectonic Setting. Geological Society of America -Special Paper Vol. 265, pp. 233–243.

De la Cruz, J., Herrera, I., 2000. Mapa geológico del cuadrángulo de Characato, a escala 1: 50000. Instituto Geológico Minero y Metalúrgico (INGEMMET), Lima, Perú .

de Silva, S.L., Francis, P.W., 1991. Volcanoes of the Central Andes. Springer-Verlag, New York (216 pp.).

de Silva, S.L., Zandt, G., Trumbull, R., Viramonte, J., Salas, G., Jimenez, N., 2006. Large ignimbrite eruptions and volcano-tectonic depressions in the Central Andes: a thermomechanical perspective. In: Troise, C., De Natale, G., Kilburn, C.R.J. (Eds.), Mechanisms of Activity and Unrest at Large CalderasGeological Society Special Publication No. 269. The Geological Society, London, pp. 47–63.

Defant, M.J., Drummond, M.S., 1990. Derivation of some modern arc magmas by melting of young subducted lithosphere. Nature 347, 662–665.

Delacour, A., Gerbe, M.-C., Thouret, J.-C., Worner, G., Paquereau, P., 2007. Magma evolution of Quaternary minor volcanic centres in Southern Peru, Central Andes. Bulletin of Volcanology 69, 581–608.

Delaite, G., Thouret, J.-C., Sheridan, M.F., Stinton, A., Labazuy, P., Souriot, T., van Westen, C., 2005. Assessment of volcanic hazards of El Misti and in the city of Arequipa, Peru, based on GIS and simulations, with emphasis on lahars. Zeitschrift fur Geomorphology Neue Folge Supplementbände 140, 209–231.

DePaolo, D.J., 1981. Trace element and isotopic effects of combined wallrock assimilation and fractional crystallization. Earth and Planetary Science Letters 53, 89–202.

DePaolo, D.J., 1988. Neodymium Isotope Geochemistry. Springer-Verlag, Berlin, West Germany (187 pp.).

Drummond, M.S., Defant, M.J., 1990. A model for trondhjemite-tonalite-dacite genesis and crustal growth via slab melting: Archean to modern comparisons. Journal of Geophysical Research 95 (B13), 21503–21521.

Erdmann, S., Martel, C., Pichavant, M., Kushnir, A., 2014. Amphibole as an archivist of magmatic crystallization conditions: problems, potential, and implications for inferring magma storage prior to the paroxysmal 2010 eruption of Mount Merapi, Indonesia. Contributions to Mineralogy and Petrology 167:1016. http://dx.doi.org/10.1007/s00410-014-1016-4.

Ewart, A., Griffin, W.L., 1994. Proton-microprobe trace element study of selected Leg 135 core samples. In: Hawkins, J., Parson, L., Allan, J., et al. (Eds.), Proceedings of the Ocean Drilling Program, Scientific Results, College Station, TX (Ocean Drilling Program) Vol. 135, pp. 533–542.

Faure, G., 1977. Principles of Isotope Geology. J. Wiley & Sons, New York (589 pp.).

Feeley, T.C., Davidson, J.P., 1994. Petrology of the calc-alkaline lavas at Volcán Ollagüe and the origin of compositional diversity at Central Andean strato-volcanoes: an example from volcan Ollagüe, Andean central volcanic zone. Journal of Petrology 35, 1295–1340.

Fourcade, S., Allègre, C.J., 1981. Trace element behaviour in granite genesis: a case study - the calc-alkaline plutonic association from Quérigut complex (Pyrénées, France). Contributions to Mineralogy and Petrology 76, 177–195.

Gerbe, M.-C., Thouret, J.-C., 2004. Role of magma mixing in the petrogenesis of lavas erupted through the 1990-98 explosive activity of Nevado Sabancaya, southern Peru. Bulletin of Volcanology 66, 541–561.

Godoy, B., Wörner, G., Kojima, S., Aguilera, F., Simnon, K., 2014. Low-pressure evolution of arc magmas in thickened crust: the San Pedro-Linzor volcanic chain, Central Andes, Northern Chile. Journal of South American Earth Sciences 52, 24–42.
Green, T.H., Adam, J., 2003. Experimentally determined trace element characteristics of aqueous fluid from partially dehydrated mafic oceanic crust at 3.0 GPa, 650–700 C. European Journal of Mineralogy 15, 815–830.
Guevara, C., 1969. Geología del cuadrángulo de Characato. Boletín del Servicio Geológico de Minería N° 23, Lima .
Hammarstrom, J.M., Zen, E., 1986. Aluminium in hornblende: an empirical igneous geobarometer. American Mineralogist 71, 1297–1313.
Harker, A., 1909. The Natural History of Igneous Rocks. Methuen and Co, London (379 pp.).
Harmon, R.S., Hoefs, J., 1984. Oxygen isotope ratios in late Cenozoic Andean volcanics. In: Harmon, R.S., Barreiro, B.A. (Eds.), Andean Magmatism. Chemical and Isotopic Constraints. Shiva Publishing Limited, pp. 9–19.
Harmon, R.S., Thorpe, R.S., Francis, P.W., 1981. Petrogenesis of Andean andesites from combined O-Sr relationship. Nature 290, 396–399.
Harmon, R.S., Barreiro, B.A., Moorbath, S., Hoefs, J., Francis, P.W., Thorpe, R.S., Déruelle, B., McHugh, J., Viglino, J.A., 1984. Regional O-, Sr-, and Pb-isotope relationships in late Cenozoic calc-alkaline lavas of the Andean Cordillera. Journal of the Geological Society of London 141 (5), 803–822.
Harpel, C., de Silva, S., Salas, G., 2011. The 2 ka Eruption of Misti Volcano, Southern Peru—The Most Recent Plinian Eruption of Arequipa's Iconic Volcano. Geological Society of America Special papers Vol. 484 (72 pp.).
Haschke, M.R., Siebel, W., Günther, A., Scheuber, E., 2002. Repeated crustal thickening and recycling during the Andean orogeny in North Chile (21°–26°S). Journal of Geophysical Research 107:1–18. http://dx.doi.org/10.1029/2001JB000328.
Haschke, M., Günther, A., Melnick, D., Echtler, H., Reutter, K.-J., Scheuber, E., Oncken, O., 2006. Central and Southern Andean tectonic evolution inferred from arc magmatism. In: Oncken, O., Chong, G., Franz, G., Giese, P., Götze, H.-J., Ramos, V.A., Strecker, M.R., Wigger, P. (Eds.), The Andes Active Subduction OrogenyFrontiers in Earth Sciences vol. 1. Springer, Heidelberg, Berlin, Germany, pp. 337–353.
Herron, E.M., 1972. Sea-floor and the Cenozoic history of the East Central Pacific. Geological Society of America Bulletin 83, 1671–1692.
Hildreth, W., Moorbath, S., 1988. Crustal contributions to arc magmatism in the Andes of Central Chile. Contributions to Mineralogy and Petrology 98, 455–489.
Hoffer, G., 2008. Fusion partielle d'un manteau métasomatisé par un liquide adakitique: Approches géochimique et expérimentale de la genèse et de l'évolution des magmas de l'arrière-arc équatorien. Unpub. PhD Thesis. Université Blaise Pascal, Clermont-Ferrand, France 320 pp.
Hollister, L.S., Grissom, G.C., Peters, E.K., Stowell, H.H., Sisson, V.B., 1987. Confirmation of the empirical correlation of Al in hornblende with pressure of solidification of calc-alkaline plutons. American Mineralogist 72, 231–239.
James, D.E., 1982. A combined O, Sr, Nd, and Pb isotopic and trace element study of crustal contamination in central Andean lavas, I. Local geochemical variations. Earth and Planetary Science Letters 57, 47–62.
James, D.E., 1984. Quantitative models for crustal contamination in the Central and Northern Andes. In: Harmon, R.S., Barreiro, B.A. (Eds.), Andean Magmatism. Chemical and Isotopic Constraints. Shiva Publishing Limited, pp. 124–138.
Janoušek, V., Moyen, J.-F., Martin, H., Erban, V., Farrow, C., 2015. Geochemical Modelling of Igneous Processes: Principles and Recipes in R Language. Bringing the Power of R to a Geochemical Community. Springer Geochemistry. Springer-Verlag, Berlin and Heidelberg, 345 pp.
Kawamoto, T., 1992. Dusty and honeycomb plagioclase: indicator of processes in the Uchino stratified magma chamber, Izu peninsula, Japan. Journal of Volcanology and Geothermal Research 49, 191–280.
Kay, S.M., 2002. Andean adakites from slab melting, crustal thickening, and fore-arc subduction erosion. 5th International Symposium of Andean Geodynamics, pp. 405–408.
Kay, S.M., Mpodosiz, C., Coira, B., 1999. Neogene magmatism, tectonics, and mineral deposits of the Central Andes (22 to 33° S). In: Skinner, B.S. (Ed.), Geology and Ore Deposits of the Central Andes. Society of Economic Geological Special Publication Vol. 7, pp. 27–59.
Kay, S.M., Coira, B., Caffe, P.J., Chen, C.-H., 2010. Regional chemical diversity, crustal and mantle sources and evolution of central Andean Puna plateau ignimbrites. Journal of Volcanology and Geothermal Research 198, 81–111.
Kiebala, A., 2008. Magmatic Processes by U-Th Disequilibria Method. Comparison of Two Andean Systems: El Misti Volcano (S. Peru) and Taapaca Volcanic Center (N. Chile). (PhD. Thesis). Georg-August-Universität Göttingen, Germany (93 pp.).
Kiss, B., Harangi, S., Ntaflos, T., Mason, P.R.D., Pál-Molnár, E., 2014. Amphibole perspective to unravel pre-eruptive processes and conditions in volcanic plumbing systems beneath intermediate arc volcanoes: a case study from Ciomadul volcano (SE Carpathians). Contributions to Mineralogy and Petrology 167:986. http://dx.doi.org/10.1007/s00410-014-0986-6.
Kono, M., Fukao, Y., Yamamoto, A., 1989. Mountain building in the Central Andes. Journal of Geophysical Research 94 (B4), 3891–3905.
Leake, B.E., Woolley, A.R., Arps, C.E.S., Birch, W.D., Gilbert, M.C., Grice, J.D., Hawthorne, F.C., Kato, A., Kish, H.J., Krivovichev, V.G., Linthout, K., Laird, J., Mandarino, J., Maresch, W.V., Nickel, E.H., Schumaker, J.C., Smith, D.C., Stephenson, N.C.N., Ungaretti, L., Whittaker, E.J.W., Youzhi, G., 1997. Nomenclature of amphiboles; report of the subcommittee on amphiboles of the International Mineralogical Association Commission on New Minerals and Mineral Names. The Canadian Mineralogist 35, 219–246.
Leeman, W.P., Hawkesworth, C.J., 1986. Open magma systems: trace element and isotopic constraints. Journal of Geophysical Research 91, 5901–5912.
Lefèvre, C., 1979. Un exemple de volcanisme de marge active dans les Andes du Pérou (sud) du Miocène à l'actuel (zonation et pétrogenèse des andésites et shoshonites) Unpub. Thèse de doctorat d'Etat, Université sciences et techniques du Languedoc. 555 pp. (in French).
Legendre, C., 1999. Pétrogenèse du volcan "Misti Moderne" (Sud Pérou): essai de caractérisation de l'évolution pétro-géochimique et chronologique (Mémoire de fin d'étude de l'Institut Géologique Albert de Lapparent, France, 88 pp.).
Legros, F., 2001. Tephra stratigraphy of Misti volcano, Peru. Journal of South American Earth Sciences 14, 15–29.
Loewy, S.L., Connelly, J.N., Dalziel, I.W.D., 2004. An orphaned basement block: the Arequipa-Antofalla Basement of the central Andean margin of South America. Geological Society of America Bulletin 166, 171–187.
Macpherson, C.G., Dreher, S.T., Thirwall, M.F., 2006. Adakites without slab melting: high pressure differentiation of island arc magma, Mindanao, the Philippines. Earth and Planetary Science Letters 243, 581–593.
Mahood, G., Hildreth, W., 1983. Large partition coefficients for trace elements in high-silica rhyolites. Geochimica et Cosmochimica Acta 47, 11–30.
Mamani, M., Tassara, A., Wörner, G., 2008. Composition and structural control of crustal domains in the Central Andes. Geochemistry, Geophysics, Geosystems 9 (3). http://dx.doi.org/10.1029/2007GC001925.
Mamani, M., Wörner, G., Sempéré, T., 2010. Geochemical variation in igneous rocks of the Central Andean orocline (13 °S to 18 °S): tracing crustal thickening and magmas generation through time and space. Geological Society of America Bulletin 97, 241–254.
Martin, H., 1986. Effect of steeper Archaean geothermal gradient on geochemistry of subduction-zone magmas. Geology 14, 753–756.
Martin, H., 1987. Archaean and modern granitoids as indicators of changes in geodynamic processes. Revista Brasileira de Geociencias 17, 360–365.
Martin, H., 1999. Adakitic magmas: modern analogues of Archaean granitoids. Lithos 46, 411–429.
Martin, H., Smithies, R.H., Rapp, R., Moyen, J.-F., Champion, D., 2005. An overview of adakite, tonalite-tronhjemite-granodiorite (TTG), and sanukitoid: relationships and some implications for crustal evolution. Lithos 79 (1–2), 1–24.
Martin, E., Martin, H., Sigmarsson, O., 2010. Continental geochemical signatures from Iceland and implications for models of early Archaean crust formation: comment. Earth and Planetary Science Letters 293:218–219. http://dx.doi.org/10.1016/j.epsl.2010.02.021.
Monzier, M., Robin, C., Eissen, J.P., Cotten, J., 1997. Geochemistry vs. seismo-tectonics along the volcanic New Hebrides Central Chain (Southwest Pacific). Journal of Volcanology and Geothermal Research 78 (1–2), 1–29.
Morimoto, N., Fabries, J., Ferguson, A.K., Ginzburg, I.V., Ross, M., Seifert, F.A., Zussman, J., 1988. Nomenclature of pyroxenes. American Mineralogist 73, 1123–1133.
Moyen, J.-F., 2009. High Sr/Y and La/Yb ratios: the meaning of the "adakitic signature". Lithos 112, 556–574.
Nash, W.P., Crecraft, H.R., 1985. Partition coefficients for trace elements in silicic magmas. Geochimica et Cosmochimica Acta 49, 2309–2322.
Norabuena, E., Leffler-Griffin, L., Mao, A., Dixon, T., Stein, S., Sacks, I.S., Ocola, L., Ellis, M., 1998. Space geodetic observation of Nazca-South America convergence across Central Andes. Science 279, 358–362.
Paquereau-Lebti, P., Thouret, J.-C., Wörner, G., Fornari, M., 2006. Neogene and Quaternary ignimbrites in the area of Arequipa, southern Peru: stratigraphical and petrological correlations. Journal of Volcanology and Geothermal Research 154, 251–275.
Patiño Douce, A.E., 1993. Ti substitution in biotite: an empirical model with applications to thermometry, O_2 and H_2O barometries, and consequences for biotite stability. Chemical Geology 108, 133–162.
Peacock, S.M., Rushmer, T., Thompson, A.B., 1994. Partial melting of subducting oceanic crust. Earth and Planetary Science Letters 121, 227–244.
Peccerillo, P., Taylor, S.R., 1976. Geochemistry of Eocene calc-alkaline volcanic rocks from the Kastamonu area. Northern Turkey. Contributions to Mineralogy and Petrology 58, 63–81.
Pin, C., Bassin, C., 1992. Evaluation of a Sr-specific extraction chromatographic method for isotopic analyses in geological materials. Analytica Chimica Acta 269, 249–255.
Pin, C., Briot, D., Bassin, C., Poitrasson, F., 1994. Concomitant separation of strontium and samarium-neodymium for isotopic analysis in silicate samples, based on specific extraction chromatography. Analytica Chimica Acta 298, 209–217.
Putirka, K.D., 2008. Thermometers and barometers for volcanic systems. In: Putirka, K.D., Tepley, F.J. (Eds.), Minerals, Inclusions and Volcanic Processes. Reviews in Mineralogy and Geochemistry vol. 69, pp. 61–120.
Ramos, V.A., 2008. The basement of the Central Andes: the Arequipa and related terranes. Annual Review of Earth and Planetary Sciences 36, 289–324.
Rapp, R.P., Shimizu, N., Norman, M.D., Applegate, G.S., 1999. Reaction between slab-derived melts and peridotite in the mantle wedge: experimental constraints at 3.8 GPa. Chemical Geology 160, 335–356.
Rapp, R.P., Norman, M.D., Laporte, D., Yaxley, G.M., Martin, H., Foley, S.F., 2010. Continent formation in the Archean and chemical evolution of the cratonic lithosphere: melt-rock reaction experiments at 3-4 GPa and petrogenesis of Archean Mg-diorites (Sanukitoids). Journal of Petrology 51, 1237–1266.
Rayleigh, J., 1896. Theorical considerations respecting the separation of gases by diffusion and similar processes. Philosophical Magazine 42, 77–107.
Ridolfi, F., Renzulli, A., Puerini, M., 2010. Stability and chemical equilibrium of amphibole in cal-alkaline magmas: an overview, new thermobarometric formulations and application to subduction-related volcanoes. Contributions to Mineralogy and Petrology 160, 45–66.
Rivera, M., 2010. Genèse et évolution des magmas andésitiques à rhyodacitiques récents des volcans Misti et Ubinas (Sud du Pérou) Unpub. PhD Thesis, Blaise Pascal University (France). 407 pp (in French).
Rivera, M., Thouret, J.C., Samaniego, P., Le Pennec, J.L., 2014. The 2006-2009 activity of Ubinas volcano (Peru): petrology of the 2006 eruptive products and insights into genesis of andesite magmas, magma recharge and plumbing system. Journal of

Volcanology and Geothermal Research 270:122–141. http://dx.doi.org/10.1016/j.jvolgeores.2013.11.010.
Rogers, N.W., Setterfield, T.N., 1994. Potassium and incompatible-element enrichment in shoshonitic lavas from the Tavua Volcano, Fiji. Chemical Geology 118, 43–62.
Ruprecht, P., Wörner, G., 2007. Variable regimes in magma systems documented in plagioclase zoning patterns: El Misti strato-volcano and Andahua monogenetic cones. Journal of Volcanology and Geothermal Research 165, 142–162.
Ruscitto, D.M., Wallace, P.J., Kent, A.J.R., 2011. Revisiting the compositions and volatile contents of olivine-hosted melt inclusions from the Mount Shasta region: implications for the formation of high-Mg andesites. Contributions to Mineralogy and Petrology 162:109–132. http://dx.doi.org/10.1007/s00410-010-0587-y.
Rutherford, M.J., Hill, P.M., 1993. Magma ascent rates from amphibole breakdown: an experimental study applied to the 1980-1986 Mount St. Helens eruptions. Journal of Geophysical Research 90 (B11), 19667–19685.
Schmidt, M.W., 1992. Amphibole composition in tonalite as a function of pressure; an experimental calibration of the Al-in-hornblende barometer. Contributions to Mineralogy and Petrology 110, 304–310.
Scott, J.A.J., Mather, T.A., Pyle, D.M., Rose, W.I., Chigna, G., 2012. The magmatic plumbing system beneath Santiaguito volcano, Guatemala. Journal of Volcanology and Geothermal Research 237-238, 54–68.
Sébrier, M., Soler, P., 1991. Tectonics and magmatism in the Peruvian Andes from late Oligocene time to the Present. Geological Society of America, Special Paper 265, 259–277.
Shane, P., Smith, V.C., 2013. Using amphibole crystals to reconstruct magma storage temperatures and pressures for the post-caldera collapse volcanism at Okataina volcano. Lithos 156-159, 159–170.
Siebert, L., Simkim, T., Kimberley, P., 2011. Volcanoes of the World. Third edition. Smithsonian Institution, Washington, University of California, p. 537.
Sisson, T.W., 1991. Pyroxene-high silica rhyolite trace elements partition coefficients measured by ion microprobe. Geochimica et Cosmochimica Acta 55, 1575–1585.
Sisson, T.W., 1994. Hornblende-melt trace-element partitioning measured by ion microprobe. Chemical Geology 117 (1–4), 331–344.
Sisson, T.W., Grove, T.L., 1993. Experimental investigations of the role of H_2O in calc-alkaline differentiation and subduction zone magmatism. Contributions to Mineralogy and Petrology 113, 143–166.
Sorbadère, F., Schiano, P., Métrich, N., Bertagnini, A., 2013. Small-scale coexistence of island-arc- and enriched-MORB-type basalts in the Central Vanuatu arc. Contributions to Mineralogy and Petrology 166:1305–1321. http://dx.doi.org/10.1007/s00410-013-0928-8.
Sørensen, E.V., Holm, P.M., 2008. Petrological inferences on the evolution of magmas erupted in the Andahua Valley, Peru (Central Volcanic Zone). Journal of Volcanology and Geothermal Research 177, 378–396.
Stern, C.R., 2004. Active Andean volcanism: its geologic and tectonic setting. Revista Geologica de Chile 31, 161–206.
Stern, R.J., 2010. The anatomy and ontogeny of modern intra-oceanic arc systems. Geological Society of London, Special Publication 338, 7–34.
Störmer, J.-C., Nicholls, J., 1978. Xlfrac: a program for the interactive testing of magmatic differentiation models. Computers and Geosciences 4, 143–159.
Sun, S., McDonough, W.F., 1989. Chemical and Isotopic Systematics of Oceanic Basalts: Implications for Mantle Composition and Processes. Magmatism in the Ocean Basin, Geological Society of America, Special Paper Vol. 42 pp. 313–345.
Suni, J., 1999. Estudio geológico y vulcanológico del volcán Misti y sus alrededores. Geological engineer thesis (Unpubl.). National University of San Agustin, Arequipa - Peru 179 pp. (in Spanish).
Syracuse, E.M., van Keken, P., Abers, G.A., 2010. The global range of subduction zone thermal models. Physics of the Earth and Planetary Interiors 183 (1–2), 73–90.
Tamura, Y., Yuhara, M., Ishii, T., 2000. Primary arc basalts from Daisen volcano, Japan: equilibrium crystal fractionation versus disequilibrium fractionation during supercooling. Journal of Petrology 41, 431–448.
Tepley, F.J., de Silva, S., Salas, G., 2013. Magma dynamics and petrological evolution leading to the VEI 5 2000 BP eruption of El Misti volcano, southern Peru. Journal of Petrology 54 (10), 2033–2065.
Thornburg, T.M., Kulm, L.D., 1987. Sedimentation in the Chile Trench; depositional morphologies, lithofacies, and stratigraphy. Geological Society of America Bulletin 98, 33–52.
Thorpe, R.S., Francis, P.W., Hammil, M., Baker, M.B., 1982. The Andes. In: Thorpe, R.S. (Ed.), Andesites, pp. 187–205.
Thorpe, R.S., Francis, P.W., Callaghan, O.L., 1984. Relative roles of source composition, fractional crystallization and crustal contamination in the petrogenesis of Andean volcanic rocks. In: Moorbath, S., Thompson, A.B., Oxburgh, E.R. (Eds.), The Relative Contributions of Mantle, Oceanic Crust and Continental Crust to Magma Genesis. Series A: Mathematical and Physical Sciences, Philosophical Transactions of the Royal Society of London vol. 310, pp. 675–692.
Thouret, J.-C., Finizola, A., Fornari, M., Suni, J., Legeley-Padovani, A., Frechen, M., 2001. Geology of El Misti volcano nearby the city of Arequipa, Peru. Geological Society of America Bulletin 113 (12), 1593–1610.
Thouret, J.-C., Rivera, M., Worner, G., Gerbe, M., Finizola, A., Fornari, M., Gonzales, K., 2005. Ubinas: the evolution of the historically most active volcano in southern Peru. Bulletin of Volcanology 67, 557–589.
Tosdal, R.M., 1996. The Amazon-Laurentian connection as viewed from the Middle Proterozoic rocks in the Central Andes, western Bolivia and northern Chile. Tectonics 15, 827–842.
Tropper, P., Manning, C.E., 2005. Very low solubility of rutile in H_2O at high pressure and temperature, and its implications for Ti mobility in subduction zones. American Mineralogist 90, 502–505.
Vatin-Pérignon, N., Olivier, R.A., Goemans, P., Keller, F., Briqueu, L., Salas, G., 1992. Geodynamic interpretations of plate subduction in the northernmost part of the Central Volcanic Zone from the geochemical evolution and quantification of the crustal contamination of the Nevado Solimana volcano, southern Peru. Tectonophysics 205, 329–355.
Walker Jr., B., Klemetti, E., Grunder, A., Dilles, J., Tepley, F., Giles, D., 2013. Crystal reaming during the assembly, maturation, and waning of an eleven-million-year crustal magma cycle: thermobarometry of the Aucanquilcha Volcanic Cluster. Contributions to Mineralogy and Petrology 165 (4), 663–682.
Wass, S.Y., 1979. Multiple origins of clinopyroxene in alkalic basaltic rocks. Lithos 12, 115–132.
Wasteneys, H.A., Clark, A.H.F., Langridege, R.J., 1995. Grenvillian granulite-facies metamorphism in the Arequipa Massif, Peru. Earth and Planetary Science Letters 132, 63–73.
Whitman, D., Isacks, L.B., Kay, S.M., 1996. Lithospheric structure and along-strike segmentation of the Central Andean Plateau; seismic Q, magmatism, flexure, topography and tectonics. In: Dewey, J.F., Lamb, S.H. (Eds.), Geodynamic of the Andes. Tectonophysics Vol. 259, pp. 29–40.
Whitney, D.L., Evans, B., 2010. Abbreviations for names of rock-forming minerals. American Mineralogist 95, 185–187.
Wilson, M., 1989. Igneous Petrogenesis. A Global Tectonic Approach. Chapter 7: Active Continental Margins. Unwin Hyman, London, pp. 191–225.
Wörner, G., Harmon, R.S., Davidson, J., Moorbath, S., Turner, D., McMillan, N., Nye, C., Lopez-Escobar, L., Moreno, H., 1988. The Nevados de Payachata volcanic region (18°S/69°W, N. Chile). I. Geological, geochemical and isotopic observations. Bulletin of Volcanology 50, 287–303.
Wörner, G., Moorbath, S., Harmon, R.S., 1992. Andean Cenozoic volcanic centers reflect basement isotopic domains. Geology 20, 1103–1106.
Wörner, G., Hammerschmidt, K., Henjes-Kunst, F., Lezaun, J., Wilke, H., 2000. Geochronology (40Ar/39Ar, K-Ar and He-exposure ages) of Cenozoic magmatic rocks from northern Chile (18-22°S): implications for magmatism and tectonic evolution of the Central Andes. Revista Geologica de Chile 27 (2), 205–240.